

Cosmology of Inelastic Self-Interacting Dark Matter: Linear Evolution and Observational Constraints

Xin-Chen Duan,^{a,b} Yue-Lin Sming Tsai^{a,b} and Ziwei Wang^{c,a}

^aKey Laboratory of Dark Matter and Space Astronomy,
Purple Mountain Observatory, Chinese Academy of Sciences, Nanjing 210008, China

^bSchool of Astronomy and Space Science,
University of Science and Technology of China, Hefei, Anhui 230026, China

^cDepartment of Strategic and Advanced Interdisciplinary Research, Pengcheng Laboratory,
Shenzhen, Guangdong 518066, China

E-mail: xcdan@pmo.ac.cn, smingtsai@pmo.ac.cn, wangzw@pcl.ac.cn

Abstract. We study the linear cosmological evolution of inelastic self-interacting dark matter in a two-component dark sector with a small mass splitting, assuming thermal initial conditions for the two species. We derive the coupled background and perturbation equations for inelastic conversion between the two species, considering both Power-law and Low-velocity saturation cross sections. Exothermic conversion injects kinetic energy into the light component, generating pressure support that suppresses small-scale structure and produces dark acoustic oscillations in the matter power spectrum. The resulting cutoff at scale $k > 1 h \text{Mpc}^{-1}$ depends on the normalization and velocity dependence of the cross section, the dark matter mass and the mass splitting. Using linear power spectra computed with a modified Boltzmann solver, we apply recast constraints from Lyman- α forest data and high-redshift UV luminosity functions, finding non-monotonic but closed exclusion regions driven by the competition between efficient conversion and rapid depletion of the heavy component. These results show that the internal thermodynamics of a secluded multi-component dark sector can leave observable imprints on structure formation, providing a complementary probe of dark matter beyond Standard Model interactions.

Contents

1	Introduction	1
2	Evolution equations of inelastic DM	3
2.1	Inelastic DM frameworks and their conversion cross section	4
2.2	Background evolution Equations	5
2.3	Perturbation Equations	6
3	Homogeneous Evolution	7
3.1	Reaction Rate and Decoupling	8
3.2	Chemical and Thermal Evolution	9
4	Linear Structure Formation	12
4.1	Evolution of Perturbations	12
4.2	The Matter Power Spectrum	15
5	Constraints	17
5.1	Lyman- α forest	17
5.2	High- z UV luminosity functions	18
5.3	Allowed parameter space	20
6	Summary and Discussion	21
A	Appendix	23
A.1	Thermally averaged conversion rates	23
A.2	Evolution of Number Density	23
A.3	Evolution of Temperature	24
A.4	Derivation of the Linear Perturbation Equations	25
A.5	Second-Order Density Perturbation Equations	26
A.6	Sound Speed and Pressure Perturbations in the Light Sector	27

1 Introduction

The identity of dark matter (DM) remains one of the most important open questions in modern physics. On cosmological scales, the standard collisionless Cold Dark Matter (CDM) paradigm, as a cornerstone of the Λ CDM model, has achieved remarkable success in explaining the cosmic microwave background and the large-scale structure of the Universe [1–3]. However, as observational precision increases, two distinct lines of evidence from particle physics and astrophysics suggest that the dark sector is likely more complex than a single, inert, and collisionless particle.

First, from a particle physics perspective, the null results from direct detection experiments [4–7] and collider searches [8–10] challenge the traditional Weakly Interacting Massive Particle scenario. Despite experimental sensitivities reaching the neutrino floor, the lack of an observed signal strongly suggests that DM interactions with the Standard Model (SM) are highly suppressed. This motivates the exploration of hidden or secluded dark sectors [11, 12],

where DM is thermally decoupled from the SM and governed by its own internal gauge dynamics. If the dark sector is secluded and complex, it generically features a spectrum of states rather than a single particle. This mass gap fundamentally alters the interaction dynamics. However, the cosmological evolution of such sectors imposes stringent constraints. Given the tiny DM-SM interaction mandated by DM direct detection, the standard thermal paradigm for secluded sectors relies heavily on strong self-interactions to maintain thermal equilibrium within the dark sector itself [11, 13]. To avoid suppressing the matter power spectrum through the injection of dark radiation from the decay of heavier states, the mass splitting must be kept small [14, 15]. In this nearly-degenerate regime, if the dark sector maintains thermal equilibrium primarily through co-annihilation rather than SM couplings, the surviving parameter space is tightly squeezed by Big Bang Nucleosynthesis bounds and LHC missing-energy searches [16, 17]. As a result, the viable cosmological framework naturally motivates a multi-component dark sector with rich internal thermodynamics but negligible SM interactions.

Second, from an astrophysical perspective, observations on galactic and sub-galactic scales reveal structural anomalies that are difficult to reconcile with purely collisionless dynamics. CDM N -body simulations predict steep central density profiles in halos, leading to the core-cusp problem in dwarf galaxies [18, 19] and the closely related Too-Big-To-Fail problem in massive subhalos [20] (for a review, see [21]). Furthermore, galaxies with similar maximum circular velocities can exhibit markedly different inner rotation curve shapes, a spread that neither CDM-only simulations nor baryonic feedback can fully reproduce [22–24]. Self-Interacting Dark Matter (SIDM) provides a compelling and fundamental physics alternative that can naturally address both the central density and diversity problems [25, 26].

In the SIDM framework, scattering between DM particles allows for heat transfer within the halo, thermalizing the inner regions and naturally producing the observed cored profiles. However, a successful SIDM model must navigate a tight observational needle: solving dwarf galaxy anomalies requires a large self-interaction cross-section, while observations of merging galaxy clusters impose strict upper bounds on the scattering rate [27]. Consequently, the cross-section must be velocity-dependent, which can be naturally achieved by introducing a light mediator [28–30]. However, such light-mediator models generically predict sizable DM–nucleus scattering rates, which are constrained by direct detection experiments [31, 32]. Multi-component or inelastic SIDM models offer an elegant solution to this tension and provide additional phenomenological advantages [33–35]. By introducing a mass splitting between DM states, DM–nucleus scattering becomes an endothermic process, kinematically forbidden at the low velocities characteristic of the Galactic halo, thereby naturally suppressing direct detection signals while preserving large self-interaction cross-sections [35]. Moreover, the dissipative nature of inelastic scattering can accelerate gravothermal core collapse in cluster subhaloes, offering a potential resolution to the galaxy-galaxy strong lensing anomaly [36], where CDM simulations significantly underpredict the observed lensing cross-sections of cluster substructures [37, 38].

Given the above facts, inelastic interactions emerge naturally in these complex dark sectors, offering a mechanism that can simultaneously evade direct detection bounds [39–44] and resolve small-scale astrophysical tensions through velocity-dependent scattering [45, 46]. Several closely related directions have recently been explored in the literature. Dissipative SIDM loses kinetic energy through up-scattering into a heavier state followed by rapid radiative de-excitation into dark radiation. This process accelerates gravothermal core collapse by one to two orders of magnitude compared to elastic SIDM, induces cuspy inner density profiles

via cooling flows, and favors compact galaxy sizes as well as stellar disk formation [37, 47–49]. However, cluster-scale weak-lensing observations can constrain the energy loss per collision [50]. In a complementary direction, simulations of inelastic SIDM, where scattering excites or de-excites nearly degenerate internal states, have shown that exothermic down-scattering can inject sufficient energy to evaporate satellite halos around Milky Way-mass hosts [51]. The resulting velocity kicks and modified speed distributions leave distinctive signatures in halo shapes, density profiles, and substructure [52, 53]. More broadly, multi-component DM models have demonstrated that even purely gravitational couplings between species with different masses or interaction strengths can alter halo density profiles, substructure abundances, and the satellite mass function [54–57]. Additionally, a dark hydrogen-like bound state formed via a dark $U(1)$ force predicts distinct features, such as dark acoustic oscillations in the matter power spectrum [58] and the formation of rotating dark disks within Milky Way-mass halos [59]. Furthermore, they lead to enhanced subhalo survival through central density boosting, as well as cuspy density profiles in isolated dwarfs arising from efficient dark gas cooling [60, 61]. Recent work on boosted DM [62] has further shown that the annihilation of a heavier dark species into a lighter one can suppress the small-scale power spectrum and soften galactic density profiles in a manner analogous to warm dark matter (WDM), while evading conventional WDM mass constraints.

Existing simulations of multi-component or inelastic SIDM still initialize from standard CDM power spectrum, thereby neglecting the imprint of dark-sector interactions on linear structure formation. While the linear evolution has been characterized for dark-atom cosmology and boosted DM scenarios, the behavior of nearly degenerate multi-component DM in this regime has not yet been systematically investigated. In this work, we investigate the regime of two nearly degenerate DM species, χ_h and χ_l , during the linear evolution epoch. We explore the epoch that dark sectors are kinetically decoupled with SM particles. Small couplings between them are consistent with null results from DM direct detection experiments. Meanwhile, the coupling between χ_h and χ_l is kept strong enough to affect DM structure formation, yet remains within the bounds currently permitted for self-interacting DM. This setup allows us to explore the unique imprint of multi-component DM thermodynamics without the complicating effects of dark radiation injection.

The paper is organized as follows. In Sec. 2, we summarize the parameterization of the velocity-dependent cross-section for inelastic SIDM. We then derive the relevant Boltzmann and Einstein equations governing the thermal history of the universe in Sec. 3 and linear cosmological perturbations in Sec. 4. In Sec. 5, we utilize observations of the Lyman- α forest and the UV luminosity function to impose up-to-date constraints on the model. Finally, we summarize our findings and discuss future directions in Sec. 6.

2 Evolution equations of inelastic DM

In this section, we present the theoretical framework for the cosmological evolution of inelastic DM. We first introduce the inelastic DM model and the conversion processes between DM particles relevant for cosmology. Henceforth, we refer to these conversion processes simply as "conversion" unless stated otherwise. We then describe the impact of conversion on the homogeneous background evolution. Finally, we derive the linear perturbation equations governing the growth of density and velocity fluctuations, which form the basis for the cosmological predictions discussed in subsequent sections.

2.1 Inelastic DM frameworks and their conversion cross section

We consider a DM sector composed of a light component χ_l and a heavy component χ_h , with masses m_l and m_h respectively. Their mass splitting is $\Delta m = m_h - m_l$, and we require $\Delta m < m_l$. Such systems naturally arise within inelastic or excited DM frameworks [33, 34, 63, 64], as pseudo-Dirac fermions with a small Majorana mass term [65, 66], or as multiplets within a non-Abelian dark sector [12, 67–70]. Our analysis focuses on the inelastic conversion process¹ $\chi_h\chi_h \Leftrightarrow \chi_l\chi_l$, in which the mass splitting is converted into (or drawn from) kinetic energy. We assume that self-interactions within each component are sufficiently rapid to maintain approximate kinetic equilibrium.²

We parameterize the DM conversion cross section σ for the $\chi_h\chi_h \Leftrightarrow \chi_l\chi_l$ in two forms. In the limit $\Delta m/m_l \ll 1$, the exothermic process $\chi_h\chi_h \rightarrow \chi_l\chi_l$ and endothermic process $\chi_l\chi_l \rightarrow \chi_h\chi_h$ cross sections are approximately equal.

- **Power-Law Scaling:** The conversion cross section is parameterized by the velocity-dependent relation

$$\sigma_{\chi_h\chi_h \Leftrightarrow \chi_l\chi_l} \equiv \sigma_{\text{PL}} \left(\frac{v_{\text{rel}}}{c} \right)^{n-1} \quad (2.1)$$

where σ_{PL} denotes the effective interaction strength and n follows the partial-wave expansion. The case $n = 0$ corresponds to s -wave contact interactions from short-range couplings. For $n = -1$, the cross section corresponds to the standard Sommerfeld enhancement ($\sigma v \propto v^{-1}$), a type of long-range forces mediated by light bosons [12]. Finally, the steep $n = -2$ scaling describes resonant Sommerfeld enhancement near a zero-energy pole [71], serving as a phenomenological benchmark for maximal velocity enhancement.

- **Low-velocity saturation:** We consider a velocity-dependent cross section whose corresponding σv_{rel} approaches a constant plateau as $v_{\text{rel}} \rightarrow 0$, capturing the saturation behavior expected in Sommerfeld-enhanced interactions. In contrast to a pure power-law parameterization, where the interaction rate formally diverges at low velocities, realistic interactions must saturate, as required by unitarity [72] or by the finite range of the force [73]. To incorporate this behavior while maintaining analytical simplicity, we adopt a regularized form that interpolates between power-law scaling at high velocities and a constant plateau at low velocities,

$$\sigma_{\chi_h\chi_h \Leftrightarrow \chi_l\chi_l} \equiv \frac{\sigma_{\text{sat}}(c/v_{\text{rel}})}{1 + (v_{\text{rel}}/v_0)^4} \quad (2.2)$$

where v_0 denotes the characteristic velocity at which saturation sets in and σ_{sat} determines the low-velocity plateau. This functional form provides a standard analytic fit to the cross section induced by a Yukawa potential and offers a simple two-parameter characterization of the saturation behavior, allowing us to systematically explore its impact on structure formation.

¹We neglect elastic scattering $\chi_h\chi_l \leftrightarrow \chi_h\chi_l$ and retain only the conversion reaction $\chi_h\chi_h \leftrightarrow \chi_l\chi_l$, as it is the source of non-trivial cosmological effects. Such elastic scattering can redistribute momentum between the two components and smooth small-scale features induced by the conversion reaction (e.g., softening sharp cutoffs or oscillatory structure), without qualitatively altering our conclusions.

²Self-interactions for kinetic equilibrium within each component do not spoil the bounds from bullet clusters. Besides, they do not contribute linear evolution of matter power spectrum at leading order.

Benchmark	$\sigma_{\chi_h\chi_h \leftrightarrow \chi_l\chi_l}$	velocity dependence	Normalization
BP1	Eq. (2.1)	$n = 0$	$\sigma_{\text{PL}} = 10^{-31} \text{ (cm}^2\text{)}$
BP2	Eq. (2.1)	$n = -1$	$\sigma_{\text{PL}} = 10^{-36} \text{ (cm}^2\text{)}$
BP3	Eq. (2.1)	$n = -2$	$\sigma_{\text{PL}} = 10^{-43} \text{ (cm}^2\text{)}$
BP4	Eq. (2.2)	Low-velocity saturation	$\sigma_{\text{sat}} = 10^{-28} \text{ (cm}^2\text{)}$

Table 1. Benchmark points adopted in this work. The normalizations for BP2 to BP4 are set at the center of the exclusion regions derived in Sec. 5.3, while BP1 uses a normalization intended only for comparison. All benchmarks adopt $m_\ell = 100 \text{ MeV}$ and $\Delta m/m_\ell = 10^{-2}$.

Given the distinct velocity structures, a single normalization cannot produce comparable effects for all scenarios. In Table 2.1, we define a set of representative cross-section benchmarks designed to illustrate the phenomenological impact of each velocity structure. We set normalizations at the center of the exclusion regions derived in Sec. 5.3, for velocity-enhanced cross-section ($n = -1, -2$, and σ_{sat}). In comparison, we also include the s -wave cross-section (BP1).³ The mass parameters are set to $m_\ell = 100 \text{ MeV}$ and $\Delta m/m_\ell = 10^{-2}$ for all benchmarks.

2.2 Background evolution Equations

The cosmological evolution of the DM is governed by interactions between the heavy and light species. The redshift evolution of the heavy component fraction r_h satisfies

$$\frac{dr_h}{dz} = \frac{1}{H(z)} [r_h \mathcal{R}_d - (1 - r_h) \mathcal{R}_u], \quad (2.3)$$

where $H(z)$ is the Hubble parameter and

$$r_h(z) \equiv \frac{n_h(z)}{n_l(z) + n_h(z)}, \quad (2.4)$$

with n_l and n_h denoting the number densities of the light and heavy species, respectively. Here \mathcal{R}_d and \mathcal{R}_u denote the conversion rates for the exothermic process $\chi_h\chi_h \rightarrow \chi_l\chi_l$ and the endothermic process $\chi_l\chi_l \rightarrow \chi_h\chi_h$ in the collision term,

$$\mathcal{R}_d \equiv \frac{1}{1+z} \frac{\bar{\rho}_{\chi_h}}{m_{\chi_h}} \langle \sigma v \rangle_{\chi_h\chi_h \rightarrow \chi_l\chi_l}, \quad \mathcal{R}_u \equiv \frac{1}{1+z} \frac{\bar{\rho}_{\chi_l}}{m_{\chi_l}} \langle \sigma v \rangle_{\chi_l\chi_l \rightarrow \chi_h\chi_h}, \quad (2.5)$$

where $\bar{\rho}_{\chi_i}$ is the background energy density and $\langle \sigma v \rangle$ denotes the velocity-weighted thermally averaged cross section. The explicit expressions for all conversion rates are given in Appendix A.2. For the exothermic process $\chi_h\chi_h \rightarrow \chi_l\chi_l$ the thermal average is straightforward, while the endothermic process $\chi_l\chi_l \rightarrow \chi_h\chi_h$ is suppressed by the kinematic threshold $v_{\text{rel}} > 2\sqrt{2} \Delta m/m_l$.

The temperatures of the light and heavy components, T_l and T_h , evolve as

$$\frac{dT_l}{dz} = 2 \frac{T_l}{1+z} - \frac{2}{3} \frac{\mathcal{R}_d}{H(z)} \left[\Delta m + \frac{3}{2} (T_h - T_l) \right], \quad (2.6)$$

³We adopt an arbitrary normalization of $\sigma_{\text{PL}} = 10^{-31} \text{ cm}^2$, since the s -wave conversion between dark sectors alters cosmological linear perturbations negligibly.

$$\frac{dT_h}{dz} = 2\frac{T_h}{1+z} - \frac{2}{3}\frac{\mathcal{R}_u}{H(z)} \left[-\Delta m + \frac{3}{2}(T_l - T_h) \right]. \quad (2.7)$$

In both equations, the first term on the right-hand side describes adiabatic cooling due to Hubble expansion, while the second term accounts for heat exchange from particle conversions. The exothermic process deposits kinetic energy Δm per conversion into the light species, whereas the endothermic process extracts it from the light population. Note that each temperature equation involves only the conversion rate that produces particles of that species. This is because newly created particles carry kinetic energy that differs from the thermal average of the recipient population, thereby modifying its temperature, while the removal of particles from the source population does not alter the mean kinetic energy of the remaining particles at leading order.

Solving Eqs. (2.3) to (2.7) determines the homogeneous thermochemical evolution of the dark sector, including the departure from chemical and thermal equilibrium between the heavy and light species. The derivations of the number density and temperature evolution equations are presented in Appendices A.2 and A.3, respectively. The resulting redshift-dependent quantities $r_h(z)$, $T_l(z)$, and $T_h(z)$ provide the necessary background inputs for the linear perturbation equations discussed in the next section.

2.3 Perturbation Equations

To describe the growth of structure, we work in the Newtonian gauge and consider linear perturbations. The density perturbations of the two species, δ_l and δ_h , evolve as

$$\delta'_l = -\theta_l + 3\Phi' + \xi\mathcal{R}_d(2\delta_h - \delta_l + \Psi) - \mathcal{R}_u(\delta_l + \Psi), \quad (2.8)$$

$$\delta'_h = -\theta_h + 3\Phi' + \frac{1}{\xi}\mathcal{R}_u(2\delta_l - \delta_h + \Psi) - \mathcal{R}_d(\delta_h + \Psi), \quad (2.9)$$

where a prime (\prime) denotes a derivative with respect to conformal time τ , Ψ and Φ are the Bardeen potentials in the Newtonian gauge, $\theta_{l,h}$ are the velocity divergences, and $\xi \equiv \bar{\rho}_h/\bar{\rho}_l$. The corresponding momentum conservation equations are

$$\theta'_l = -\mathcal{H}\theta_l + k^2\Psi + k^2\hat{c}_{s,l}^2\delta_l + \xi\mathcal{R}_d(\theta_h - \theta_l), \quad (2.10)$$

$$\theta'_h = -\mathcal{H}\theta_h + k^2\Psi + \frac{1}{\xi}\mathcal{R}_u(\theta_l - \theta_h), \quad (2.11)$$

where $\mathcal{H} \equiv aH$ is the conformal Hubble parameter and $\hat{c}_{s,l}^2$ is the rest-frame sound speed of the light component. The derivation of the perturbation equations is presented in Appendix A.4. Under the assumption of local thermal equilibrium, we identify $\hat{c}_{s,l}^2$ with the adiabatic sound speed $c_{a,l}^2 \equiv \dot{P}_l/\dot{\rho}_l$. The detailed definition of sound speed and justification of this approximation are given in Appendix A.6. Note that the pressure term $k^2\hat{c}_{s,h}^2\delta_h$ has been omitted from Eq. (2.11), as T_h is governed solely by the endothermic process $\chi_l\chi_l \rightarrow \chi_h\chi_h$, whose cross section is kinematically suppressed at early times. Hence, T_h evolves through adiabatic cooling, yielding $\hat{c}_{s,h}^2 \equiv T_h/m_h \ll \hat{c}_{s,l}^2$, and the corresponding pressure support for the heavy component is negligible.

In the density equations (2.8) and (2.9), the terms proportional to \mathcal{R}_d and \mathcal{R}_u arise from perturbations in conversion rates and indicate how local density fluctuations affect net particle transfer between species. In the momentum equations (2.10) and (2.11), the collision terms act as a drag force that tends to equilibrate the bulk velocities of the two components. The

finite temperature of the light species further provides a pressure support through the $\hat{c}_{s,l}^2$ term that resists gravitational collapse. For sufficiently large reaction rates, the combined effect of drag and pressure support suppresses the growth of perturbations, leading to observable deviations in the matter power spectrum relative to the standard Λ CDM scenario. The resulting signatures are quantified in Sec. 4.

To solve the coupled system of background and perturbation equations, we implement the two-component DM model into the Boltzmann solver CLASS⁴, incorporating the inelastic conversion dynamics at both the background and perturbation levels. Unless otherwise stated, the standard cosmological parameters are fixed to the *Planck* 2018 best-fit values [75]: $H_0 = 67.36 \text{ km s}^{-1} \text{ Mpc}^{-1}$, $\Omega_b h^2 = 0.02237$, $\Omega_c h^2 = 0.1200$, $\ln(10^{10} A_s) = 3.044$, $n_s = 0.9649$, and $\tau_{\text{reio}} = 0.0544$, where Ω_c denotes the total DM density. In this work, we assume that the DM consists entirely of χ_l and χ_h , with $\Omega_{\chi_l} + \Omega_{\chi_h} = \Omega_c$. The dark sector is then characterized by the free parameters $\{m_l, \Delta m/m_l\}$, and the cross-section parameters: $\{\sigma_{\text{PL}}, n\}$ for the power-law scaling or $\{\sigma_{\text{sat}}, v_0\}$ for the low-velocity saturation.

3 Homogeneous Evolution

We begin the evolution at the epoch of kinetic decoupling of the dark sector from the SM plasma. Prior to this epoch, frequent momentum-exchange interactions maintain thermal contact between the dark and visible sectors, so that the dark-sector temperature tracks the photon temperature T_γ . At kinetic decoupling, the momentum-transfer rate drops below the Hubble rate, and the dark sector subsequently evolves as a thermally isolated system governed by Eqs. (2.3)–(2.7). At this point, both components share a common temperature $T_l = T_h \equiv T_{\text{init}}$, inherited from their prior thermal contact with the SM plasma.

We parametrize the initial temperature by $\eta_{\text{init}} \equiv m_l/T_{\text{init}}$ and adopt the fiducial value $\eta_{\text{init}} = 100$. This ensures that both species are deeply non-relativistic at the onset of evolution, with typical velocities $v \sim \sqrt{T/m} \sim 0.1c$, so that the non-relativistic fluid treatment underlying our Boltzmann equations is well justified. We note that the precise value of η_{init} depends on the details of the dark–SM coupling responsible for kinetic decoupling [76], and can vary over several orders of magnitude among different models. We confirm that our results are insensitive to the exact value of η_{init} , as long as it is large enough to satisfy the non-relativistic condition.

The initial fraction of the heavy component is then given by the Boltzmann ratio,

$$r_h(z = z_{\text{init}}) = \frac{n_h(z_{\text{init}})}{n_h(z_{\text{init}}) + n_l(z_{\text{init}})} = \left[1 + \exp\left(\eta_{\text{init}} \frac{\Delta m}{m_l}\right) \right]^{-1}. \quad (3.1)$$

where we have assumed equal internal degrees of freedom for both components. The initial redshift z_{init} is determined by matching the initial dark-sector temperature to the photon temperature, $T_{\text{init}} = T_\gamma(z_{\text{init}})$ ⁵. We also assume the SM and dark sector starts to kinetically decouple at z_{ini} .

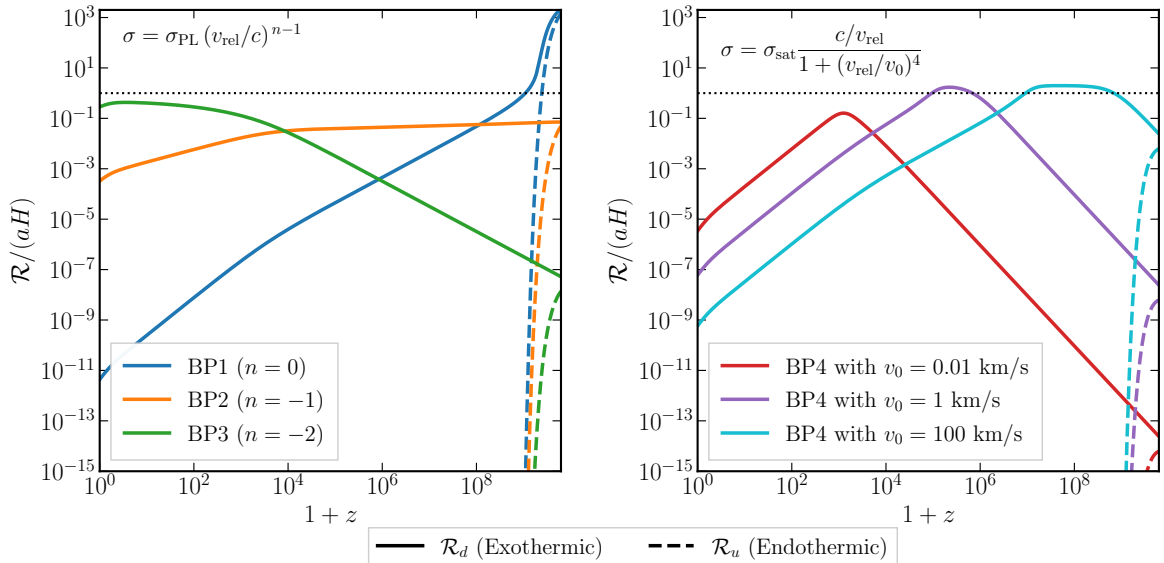


Figure 1. Ratio of the inelastic reaction rate to the Hubble rate, $\mathcal{R}/(aH)$, as a function of $1+z$ for the two cross-section parametrizations considered in this work. Solid lines denote the exothermic (down-scattering) rate \mathcal{R}_d , while dashed lines denote the endothermic (up-scattering) rate \mathcal{R}_u . The horizontal dotted line marks $\mathcal{R}/(aH) = 1$, above which inelastic conversions proceed faster than the Hubble expansion. *Left panel:* Power-law parametrization for the benchmark points BP1 ($n = 0$, blue), BP2 ($n = -1$, orange), and BP3 ($n = -2$, green) as listed in table 2.1. *Right panel:* Saturated parametrization, with $\sigma_{\text{sat}} = 10^{-28} \text{ cm}^2$ (BP4) and three representative saturation velocities: $v_0 = 0.01$ (red), 1 (purple), and 100 km/s (cyan).

3.1 Reaction Rate and Decoupling

As established by Eq. (2.3)-(2.7), the evolution of r_h is governed by the competition between conversion reaction rates and cosmic expansion, while the temperature T_l of the light component traces the interplay between adiabatic cooling and kinetic energy injection from exothermic down-scattering. For s -wave conversion ($n = 0$), light and heavy species are in thermal equilibrium with each other. In contrast, for $n < 0$ or the low-velocity saturation case, the conversion rate at early times is suppressed by the large particle velocities. Interactions between light and heavy are negligible that they experience similar adiabatic cooling from the same initial temperature. As the universe expands and DM particles slow down, the endothermic process becomes exponentially suppressed once the typical kinetic energy drops close to Δm , and the system is subsequently driven entirely by the exothermic process.

Fig. 1 illustrates the cosmological evolution of the reaction rates relative to Hubble expansion for both the power-law and low-velocity saturation scenarios. As anticipated, \mathcal{R}_u (dashed lines) drops sharply at late times, leaving \mathcal{R}_d (solid lines) to dominate the subsequent evolution.

In the case of power-law scaling (left panel), the reaction rate exhibits a sensitive de-

⁴We implement our modifications in CLASS [74] (version 3.2.5) and will make the modified code publicly available on GitHub.

⁵For a given light-particle mass m_l , the initial temperature is $T_{\text{init}} = m_l/\eta_{\text{init}}$, and the corresponding redshift follows from entropy conservation, $z_{\text{init}} = (g_{*s}(T_{\text{init}})/g_{*s,0})^{1/3} (T_{\text{init}}/T_{\gamma,0}) - 1$, where $g_{*s}(T)$ is the effective number of entropic degrees of freedom [77].

pendence on the velocity index n . Using the benchmark points defined in Table 2.1, we find that negative indices ($n < 0$) significantly enhance the interaction at low velocities, thereby sustaining efficient component conversion down to lower redshifts. Specifically, for $n = -2$, this strong low-velocity enhancement partially compensates for cosmic dilution, producing an extended plateau in the reaction rate that can persist well into the structure-formation era. By contrast, the s -wave scenario is dominated by early-time dynamics, with the reaction rate declining rapidly toward low redshifts.

For the low-velocity saturation case (right panel), the behavior is controlled by v_0 . At early times, when particle velocities are much larger than v_0 (namely, $\sigma v \propto v^{-4}$), $\mathcal{R}/(aH)$ grows rapidly as particles slow down. Once $v_{\text{rel}} \lesssim v_0$, σv saturates to σ_{sat} and the enhancement ceases. The ratio $\mathcal{R}/(aH)$ then peaks and inevitably declines, driven by the decreasing n_h , which falls both from cosmic dilution of the total number density and from depletion of r_h via exothermic conversion. A larger v_0 implies that saturation is reached at higher redshift, shifting the peak to earlier times. The width of the peak also depends on the background cosmology. Transitions occurring during radiation domination (large v_0) produce broader features than those during matter domination (small v_0), reflecting the different scaling of $H(z)$ in these two eras.

3.2 Chemical and Thermal Evolution

We now examine how inelastic conversion shapes the homogeneous evolution of the dark sector, focusing on two observables: the heavy-component fraction r_h and the light-component temperature T_l .⁶ Although both quantities are driven by the same underlying conversion process, their transition epochs generally do not coincide, as they are governed by different criteria. Once \mathcal{R}_u becomes negligible, Eq. (2.3) reduces to $d \ln r_h / dz \approx \mathcal{R}_d / H$, implying that efficient conversion from heavy species to light requires $\mathcal{R}_d \gtrsim aH$. On the other hand, a departure from adiabatic cooling occurs only when the heating term $(\mathcal{R}_d / H)[\Delta m + \frac{3}{2}(T_h - T_l)]$ in Eq. (2.6) becomes comparable to the adiabatic cooling term $2T_l / (1 + z)$. As a result, the depletion of the heavy component and the thermal departure of the light component generally begin at different redshifts. The velocity dependence of the cross section determines which process occurs first, thereby mapping the homogeneous evolution onto cross-section parameter dependencies.

Furthermore, the dependence of the homogeneous evolution on these parameters is not purely dynamical. The mass splitting $\Delta m / m_l$ not only controls the conversion dynamics but also sets the initial heavy-component fraction through the Boltzmann factor in Eq. (3.1), while m_l determines the initial temperature $T_{\text{init}} = m_l / \eta_{\text{init}}$ and z_{init} . Hence, the result of homogeneous evolution depends on the initial conditions and subsequent conversion dynamics, as shown numerically in Fig. 2 and Fig. 3.

Fig. 2 illustrates these general features for the power-law parametrization. The left and right panels show the evolution of r_h and T_l , respectively. The upper and lower panels correspond to different values of $\Delta m / m_l$ and m_l , while the shaded bands indicate the effect of the cross-section normalization. The initial redshift z_{init} is marked by the gray circles. We summarize the key points of Fig. 2 below:

- **Effect of velocity-dependence:** The velocity dependence of the cross section determines the ordering of chemical depletion and thermal departure, thereby controls the

⁶We do not track T_h separately, as the strong early suppression of \mathcal{R}_u renders the conversion term in Eq. (2.7) negligible, so that T_h follows pure adiabatic cooling throughout.

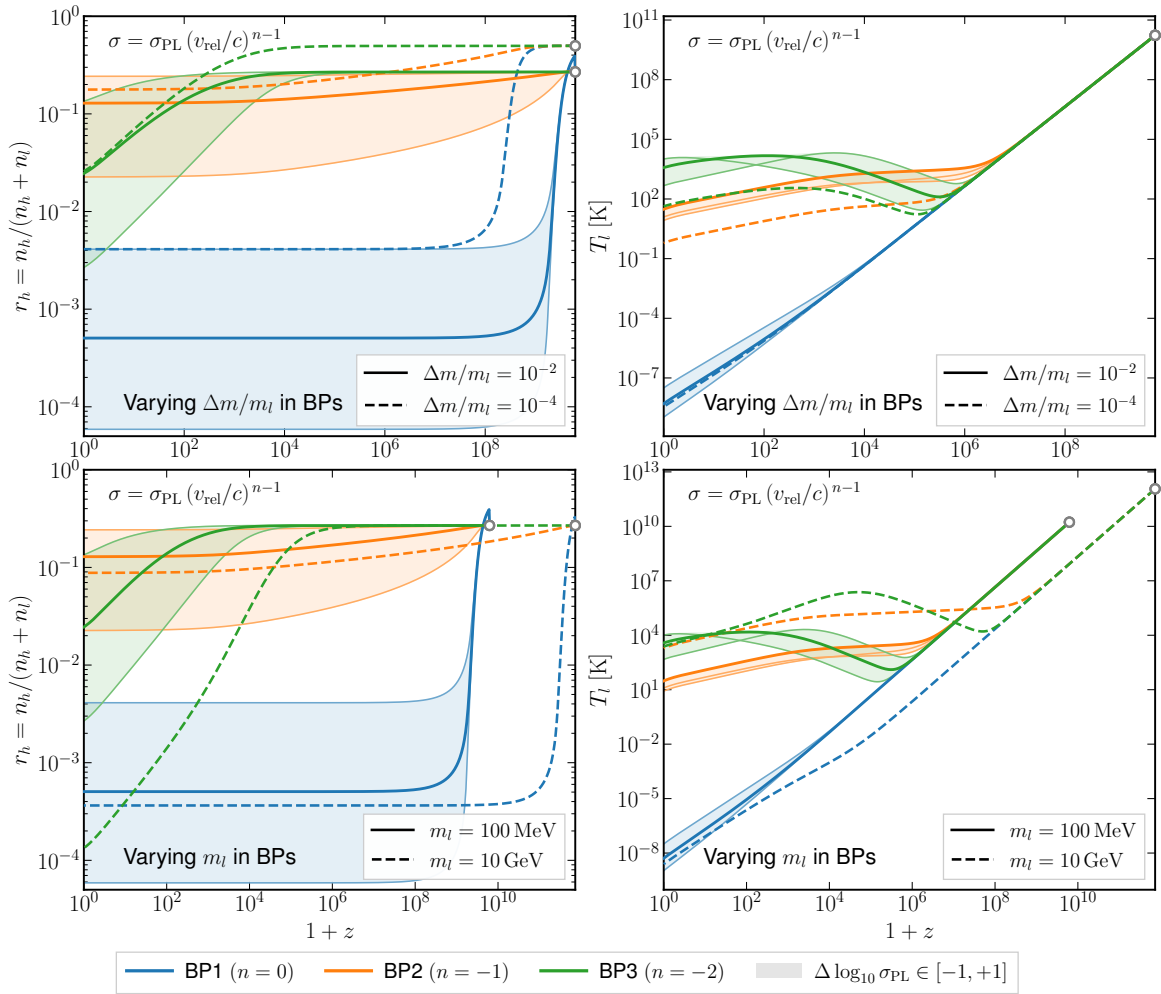


Figure 2. Homogeneous evolution of the heavy-component fraction $r_h = n_h/(n_h + n_l)$ (left column) and the light-component temperature T_l (right column) as a function of $1+z$ for the power-law cross-section parametrization. Blue, orange, and green curves correspond to BP1, BP2, and BP3 given in Table 2.1. The gray cycles mark the initial redshift z_{init} . The top row varies the mass splitting $\Delta m/m_l$ at fixed $m_l = 100$ MeV, while the bottom row varies m_l at fixed $\Delta m/m_l = 10^{-2}$. Solid lines denote the benchmark values and dashed lines the varied values. Shaded bands indicate a factor-of-ten variation of the cross section around each benchmark, $\Delta \log_{10} [\sigma_{\text{PL}}] \in [-1, +1]$.

final value of T_l .

For $n = 0$, depletion occurs before heating. The heavy component is mostly exhausted before T_l deviates from adiabatic cooling, thus heating is negligible. For $n = -2$, heating occurs before depletion. In this case T_l deviates from adiabatic cooling while a considerable heavy fraction remains, leading to a higher final T_l . The $n = -1$ case lies between these two extremes, with depletion and heating proceeding more concurrently.

- **Role of $\Delta m/m_l$:** The mass splitting plays a dual role. A larger $\Delta m/m_l$ releases more energy per conversion, but simultaneously suppresses the initial r_h through the Boltzmann factor in Eq. (3.1), reducing the total energy budget available for heating. Comparing $\Delta m/m_l = 10^{-2}$ (solid) and 10^{-4} (dashed) in the upper panels, the larger

splitting produces a higher final T_l for $n = -2$ and $n = -1$. For $n = 0$ the effect is weaker, as the heavy component is already depleted before heating becomes effective. For sufficiently large $\Delta m/m_l$, the exponential suppression of the initial r_h eventually dominates, e.g., $r_h(z_{\text{init}}) \sim 10^{-5}$ for $\Delta m/m_l = 0.1$, leading to a non-monotonic dependence of the final T_l on $\Delta m/m_l$.

- **Role of m_l :** The larger m_l raises z_{init} and T_{init} and heavy components experience chemical depletion and thermal departure from adiabatic cooling at earlier times, for different cross-sections of models. Consequently, the remnant ratio of heavy components r_h at given redshift becomes lower than the cases with smaller m_l .

The dependence of the final T_l on m_l is less straightforward. Comparing $m_l = 100$ MeV (solid) and 10 GeV (dashed) in the lower panels, the larger m_l produces a lower final r_h among all scenarios. For $n = 0$, the temperature uplift is small, so varying m_l has little effect on the final T_l . For $n = -2$, a larger m_l extends the effective heating period but simultaneously enhances the depletion of the heavy component. These two effects largely compensate, leaving the final T_l only weakly dependent on m_l . For $n = -1$, however, this compensation is incomplete, and the final T_l retains a more pronounced dependence on m_l .

- **Impact of σ_{PL} :** The cross-section normalization σ_{PL} directly controls the overall conversion strength.

A large σ_{PL} accelerates depletion, resulting in a smaller final r_h , but affects T_l non-monotonically. Such a large σ_{PL} can initiate heating earlier, yet depletes the heavy component faster, thereby cutting short the energy supply. This competition is clearly seen from $n = -2$, where the temperature curves for different σ_{PL} cross, and the highest final T_l occurs at an intermediate σ_{PL} rather than the largest one.

The homogeneous evolution for the low-velocity saturation case is shown in Fig. 3. The effects of $\Delta m/m_l$, m_l , and σ_{sat} follow the similar mechanisms discussed for the power-law case. The new feature is the saturation velocity v_0 , which determines the velocity below which the conversion rate saturates. Unlike n , which reshapes the overall evolutionary behavior, varying v_0 shifts the epoch of efficient conversion along the thermal history without qualitatively changing it. A smaller v_0 delays saturation to later times when T_l is lower, producing a stronger heating effect and preserving a larger heavy fraction, consistent with the ordering seen across the three v_0 values in Fig. 3.

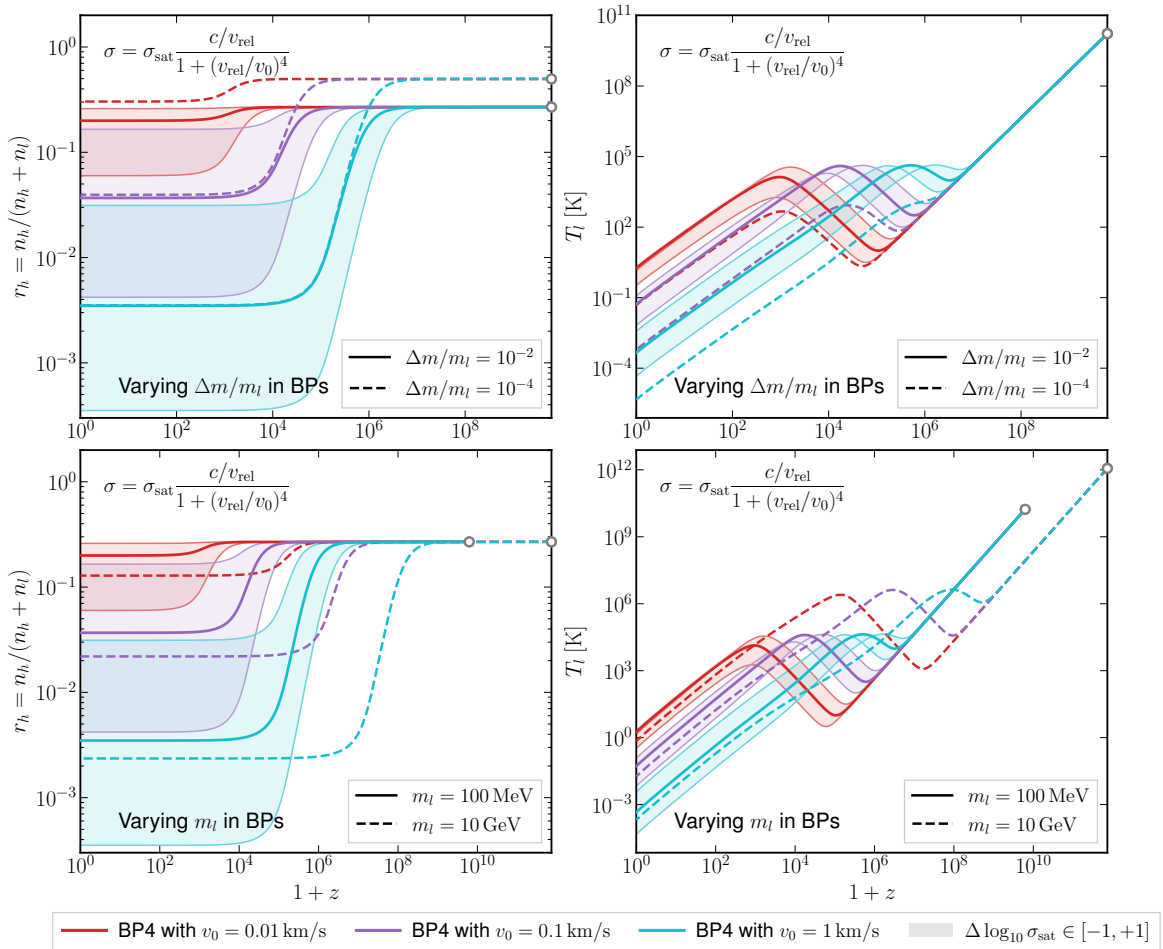


Figure 3. Analogous to Fig. 2 but for the Low-velocity saturation cross-section. Red, purple, and cyan curves correspond to saturation velocities $v_0 = 0.01, 0.1,$ and 1 km/s, respectively. We fix $\sigma_{\text{sat}} = 10^{-28}$ cm² (BP4). Shaded bands represent the cross-section normalization varying by a factor of ten, namely $\Delta \log_{10} [\sigma_{\text{sat}}] \in [-1, +1]$.

4 Linear Structure Formation

The homogeneous quantities enter Eqs. (2.8) to (2.11) and govern the perturbation evolution through gravitational growth, pressure support, and inelastic conversion. We adopt *adiabatic initial conditions*, with the dark sector perturbations initialized following the standard procedure in [78]. As implied by these background quantities, the s -wave conversion has negligible impact on structure formation. Specifically, the heavy component is depleted before relevant perturbation modes enter the horizon, and the temperature increase of the light component is too small to generate significant pressure support. Therefore, the s -wave case is not considered further.

4.1 Evolution of Perturbations

For $n < 0$ and the low-velocity saturation case, the later onset of efficient conversion can modify both the density and velocity perturbations. By eliminating the velocity divergences from the first-order equations, we obtain a set of second-order density perturbation equations

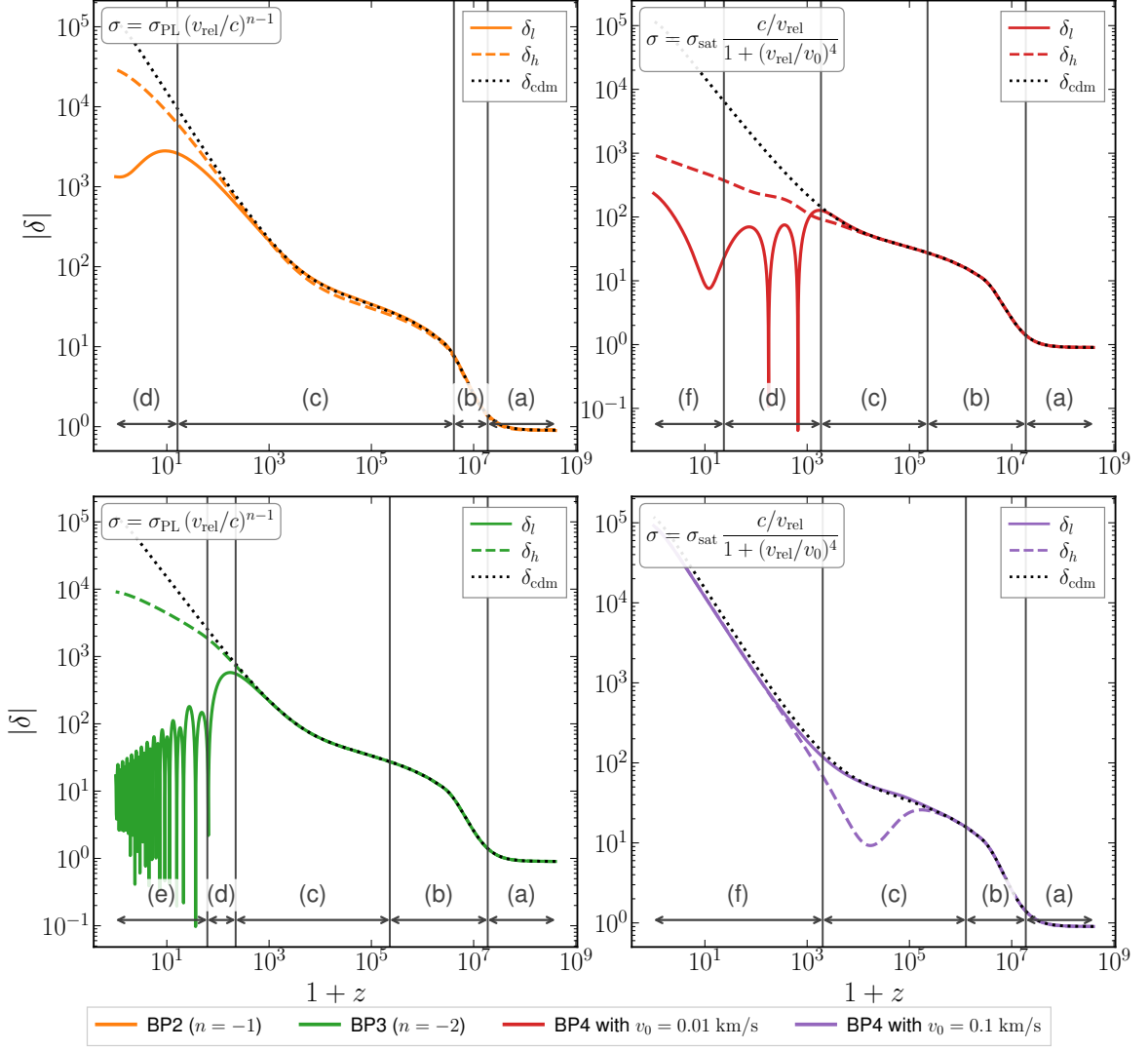


Figure 4. Evolution of the density contrasts for a representative small-scale mode $k = 60 h \text{ Mpc}^{-1}$. Solid and dashed curves show the light and heavy components δ_l and $|\delta_h|$, respectively. The dotted curve is the ΛCDM reference $|\delta_{\text{cdm}}|$. The left column uses $\sigma = \sigma_{\text{PL}}(v_{\text{rel}}/c)^{n-1}$ with $n = -1$ (upper left, BP2) and $n = -2$ (lower left, BP3), while the right column uses $\sigma = \sigma_{\text{sat}}(c/v_{\text{rel}})/[1 + (v_{\text{rel}}/v_0)^4]$ with $v_0 = 0.01 \text{ km/s}$ (upper right, BP4) and $v_0 = 0.1 \text{ km/s}$ (lower right, BP4). Labeled intervals mark the physical regimes introduced in the text: **(a)** superhorizon, **(b)** early subhorizon growth, **(c)** conversion-driven transition, **(d)** acoustic oscillation, **(e)** acoustic damping, and **(f)** late-time gravitationally dominated.

(see Appendix A.5). In these equations, the conversion process introduces additional friction terms $\mathcal{R}_d \delta'_h$ and $2\xi \mathcal{R}_d \delta'_l$ beyond the standard Hubble drag, and contributes effective mass terms proportional to δ_h and δ_l themselves, such as $(\mathcal{R}_d \mathcal{H} + \mathcal{R}'_d)\delta_h$, that directly suppress the overdensity amplitudes. The source terms S_h and S_l (Eqs. (A.40) and (A.44)) encode the gravitational response. Additionally, S_l connects to δ_h that redistributes density between the two components. To clarify the physical picture, we classify the linear perturbation evolution into six characteristic regimes based on the interplay among the conversion rate,

the wavenumber, and the Hubble expansion rate.

(a) Superhorizon Regime:

In this period, the mode is outside the horizon and satisfies $k/\mathcal{H} \ll 1$. Causality prevents any modification of the mode on these scales, preserving adiabatic initial conditions. All pressureless components share the same primordial fluctuation, thus both DM species evolve identically to standard CDM.

(b) Early Subhorizon Growth Regime:

Perturbations begin to evolve causally after entering the horizon ($k/\mathcal{H} \gtrsim 1$). The conversion rate remains much smaller than the Hubble rate. Thus all conversion-induced contributions to the perturbation equations are subdominant. Both DM species follow the adiabatic cooling and maintain small effective sound speeds. Consequently, δ_l and δ_h grow similarly to CDM.

(c) Conversion-Driven Transition Regime:

This stage begins when the effects of inelastic conversion first become important at the background level, through either the onset of heavy-component depletion or the departure of T_l from adiabatic cooling. However, the perturbation evolves more gradually: δ_l and δ_h initially grow as in CDM, then progressively diverge from CDM and from each other as the conversion terms take effect.

(d) Acoustic Oscillation Regime:

Once the pressure term $k^2 \hat{c}_{s,l}^2$ becomes comparable to the gravitational and conversion terms, δ_l develops acoustic oscillations. The competition between gravitational infall and pressure-restoring forces prevents monotonic growth, forcing δ_l to oscillate between over- and under-dense states. Therefore, the time-averaged growth rate of perturbations is much lower than the growth rate in a pressureless matter universe. This lower growth rate provides the dominant mechanism behind the suppression of the matter power spectrum on small scales. Subsequent damping further reduces the oscillation amplitude.

(e) Acoustic Damping Regime:

The friction terms in the light-component evolution equation become cumulatively important if the conversion rate remains non-negligible after oscillations begin. These contributions can be characterized by an effective damping rate $\gamma_l \equiv \frac{1}{2}(\mathcal{H} + 2\xi\mathcal{R}_d)$, which includes both Hubble drag and conversion-induced friction. When the damping rate remains smaller than the oscillation frequency, the oscillation amplitude is exponentially suppressed as

$$\delta_l \propto \exp\left[-\int^{\tau} d\tilde{\tau} \gamma_l(\tilde{\tau})\right]. \quad (4.1)$$

Since γ_l grows monotonically with the cumulative conversion history, this damping eventually produces a strong suppression of small-scale perturbations.

(f) Late Time Gravitationally Dominated Regime:

When the light-component temperature returns to adiabatic cooling and all conversion-related terms in the perturbation equations become negligible, the sound speed decreases until $k\hat{c}_{s,l}/\mathcal{H}$ falls below unity and the mode exits the oscillatory regime. Both components then resume standard gravitational growth with $\delta \propto a$ during matter domination.

Fig. 4 illustrates the linear perturbation evolution through the characteristic regimes outlined above, for a representative small-scale mode $k = 60 h \text{ Mpc}^{-1}$ using benchmarks BP2, BP3, and BP4. Solid and dashed curves show the light and heavy components $|\delta_l|$ and $|\delta_h|$, respectively, with the ΛCDM reference $|\delta_{\text{cdm}}|$ shown as the dotted curve. All four panels follow a common sequence of superhorizon evolution **(a)**, CDM-like subhorizon growth **(b)**, and a smooth departure from CDM **(c)** once inelastic conversion becomes dynamically significant. The subsequent behavior depends on the competition between the growing cross section at low velocities and the depletion of the heavy component.

For the power-law cases (left column), the evolution beyond regime **(c)** depends on how rapidly the cross section grows at low velocities. For BP3 ($n = -2$), the strong velocity enhancement sustains conversion for a sufficient duration to drive the mode through acoustic oscillations **(d)** and significant damping **(e)**, suppressing $|\delta_l|$ by several orders of magnitude relative to $|\delta_{\text{cdm}}|$. For BP2 ($n = -1$), the weaker enhancement delays the onset of acoustic oscillations to $z \sim 10$, resulting in a milder suppression of $|\delta_l|$ than $|\delta_{\text{cdm}}|$.

For the low-velocity saturation case (right column), a smaller v_0 delays the peak of the conversion rate to a later epoch where \mathcal{H} is smaller and the conversion-induced heating also produces a larger sound speed. Both effects raise $k\hat{c}_{s,l}/\mathcal{H}$ and determine whether the mode enters the oscillatory regime **(d)**, as observed for $v_0 = 0.01 \text{ km/s}$ where $|\delta_l|$ develops acoustic oscillations, but not for $v_0 = 0.1 \text{ km/s}$. In contrast to the power-law cases, the limited duration of efficient conversion in the velocity-saturation case means the mode does not enter the damping regime **(e)**, and both cases eventually recover gravitational growth **(f)** once conversion ceases.

In all scenarios, the heavy component $|\delta_h|$ remains non-oscillatory yet is suppressed relative to CDM. This suppression arises directly from the conversion process, which slows the growth of $|\delta_h|$ via additional friction $\mathcal{R}_d \delta'_h$ and effective mass terms $(\mathcal{R}_d \mathcal{H} + \mathcal{R}'_d) \delta_h$, even before light-sector oscillations begin. As $|\delta_l|$ is further suppressed, the shallower gravitational potential additionally weakens the growth of $|\delta_h|$. This correlated suppression of both components leads to a small-scale cutoff in the total matter power spectrum.

4.2 The Matter Power Spectrum

Using the Fourier mode evolution established above, we now compute the matter power spectrum to capture the scale-dependent impact of inelastic conversion. We define the squared transfer function $\mathcal{T}^2(k, z) \equiv P(k, z)/P_{\Lambda\text{CDM}}(k, z)$. The left panel of Fig. 5 shows $\mathcal{T}^2(k)$ at $z = 0$ (solid) and $z = 50$ (dashed) for BP2, BP3, and BP4 (with $v_0 = 0.01$ and 0.1 km/s). The right panel compares the $z = 0$ results with the $\mathcal{T}^2(k)$ of thermal WDM, matched at the half-mode scale $k_{1/2}$ defined by $\mathcal{T}^2(k_{1/2}) = 0.5$.

In the left panel, $n = -2$ shows the strongest suppression, setting in at $k \sim$ a few $h \text{ Mpc}^{-1}$. The $n = -1$ case and the Low-velocity saturation case with $v_0 = 0.01 \text{ km/s}$ are suppressed starting from $k \sim 10 h \text{ Mpc}^{-1}$, while $v_0 = 0.1 \text{ km/s}$ remains close to ΛCDM until $k \sim 60 h \text{ Mpc}^{-1}$. Dark acoustic oscillations (DAOs) are visible in both Low-velocity saturation cases but absent for the power-law cross sections. Comparing $z = 0$ and $z = 50$ for the two velocity-dependence cases, the power-law cases show stronger suppression at lower redshift, whereas the Low-velocity saturation cases show smoothing of the DAO features from $z = 50$ to $z = 0$.

These features are consistent with the single-mode analysis in the previous section. The larger suppression scale for $n = -2$ reflects the prolonged conversion and cumulative damping in regime **(e)**, which also erases the oscillatory structure across modes. For $n = -1$,

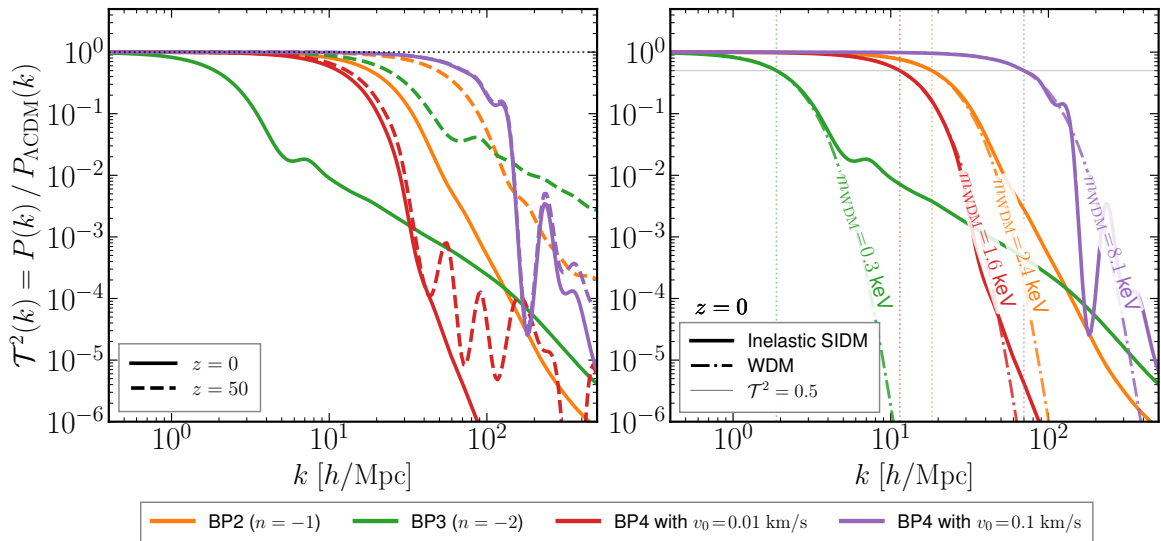


Figure 5. Squared transfer function for the benchmark models. *Left panel* shows the matter power spectrum ratio $P(k)/P_{\Lambda\text{CDM}}(k)$ at $z = 0$ (solid) and $z = 50$ (dashed) for four benchmarks $n = -1$ (BP2, orange), $n = -2$ (BP3, green), as well as saturated $v_0 = 0.01 \text{ km s}^{-1}$ (BP4, red) and $v_0 = 0.1 \text{ km s}^{-1}$ (BP4, purple). *Right panel* compares the $z = 0$ transfer functions (solid) to equivalent thermal WDM models (dot-dashed) matched at the half-mode scale $k_{1/2}$ (gray horizontal line), with vertical dotted lines marking $k_{1/2}$ for each model and the corresponding equivalent WDM mass indicated.

oscillations begin too late to develop non-negligible amplitude. In Low-velocity saturation cases, conversion ends abruptly by $z = 50$, fixing the suppression scale as well as cleanly imprinting the pressure-supported phase to produce DAOs. By contrast, power-law conversion remains active from $z = 50$ to $z = 0$, extending suppression to larger scales. The subsequent gravitational growth in regime (f) then smooths out the DAO features by $z = 0$.

In the right panel, we show the equivalent WDM masses derived by mapping the half mode scale $k_{1/2}$ of our model to the established analytical relation for a standard thermal relic WDM [79]. These equivalent masses range from $m_{\text{WDM}} \simeq 0.3 \text{ keV}$ for $n = -2$ to 8.1 keV for $v_0 = 0.1 \text{ km/s}$. The intermediate cases of $n = -1$ and $v_0 = 0.01 \text{ km/s}$ correspond to 1.6 keV and 2.4 keV respectively. At high k ($k > k_{1/2}$), the suppression tail in all inelastic SIDM cases is shallower than in their WDM counterparts. This occurs because the suppression in inelastic SIDM is driven by conversion induced heating rather than simple collisionless free streaming. Furthermore, unlike the smooth cutoff in WDM, the inelastic SIDM transfer functions feature distinct dark acoustic oscillations at high k .

Fig. 6 shows the power spectra of the light (solid lines) and heavy (dashed lines) components separately, fixing the power-law cross section at $n = -2$ and varying σ_{PL} (left), $\Delta m/m$ (center), or m_l (right) around the BP3 fiducial values. Both components remain close to unity on large scales. However, on smaller scales, the light component exhibits an earlier and sharper turnover with pronounced DAO features, due to direct pressure support from conversion-induced heating. In contrast, the heavy component shows a smoother suppression governed by its depletion history and the weakened gravitational potential.

A notable feature is the non-monotonic evolution of the power spectra. The acoustic suppression is present, and the cutoff shifts to the largest scales, at the intermediate BP3

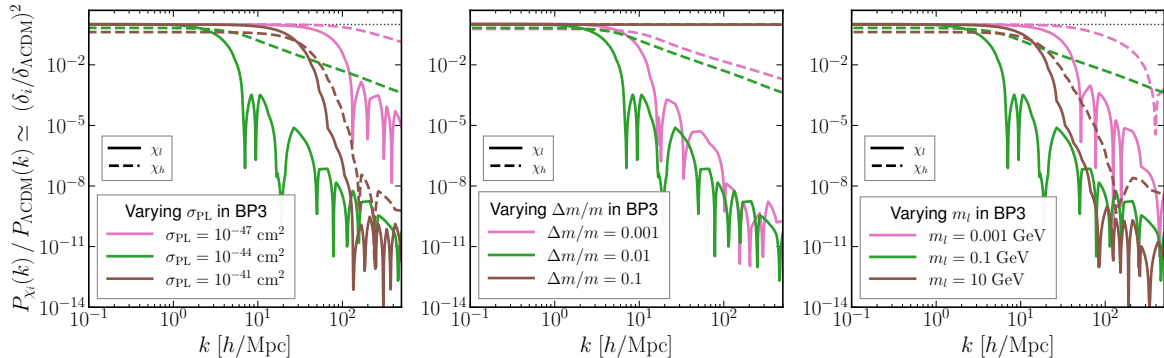


Figure 6. Parameter dependence of the linear power spectra for $\sigma = \sigma_{\text{PL}}(v_{\text{rel}}/c)^{-3}$, shown as ratios to the ΛCDM matter power spectrum at $z = 0$. The contribution of each component is approximated by $P_{\chi_i}(k) \simeq P_{\Lambda\text{CDM}}(k) [\delta_i(k)/\delta_{\Lambda\text{CDM}}(k)]^2$, with the light component χ_l in solid lines and the heavy component χ_h in dashed lines. In each panel, one parameter is varied around the BP3 fiducial values (green curves: $\sigma_{\text{PL}} = 10^{-44} \text{ cm}^2$, $\Delta m/m = 0.01$, $m_l = 0.1 \text{ GeV}$), with the other two fixed.

fiducial values (green curves). Any deviation from the reference values of σ_{PL} , $\Delta m/m$, or m_l weakens the suppression and shifts the cutoff to smaller scales. This behavior reflects the combined effects of the total energy available for conversion, the timing and duration of the heating episode, and the persistence of the resulting pressure support. A very small σ_{PL} results in inefficient conversion, while an excessively large value causes early depletion of the heavy species and shortens the effective heating period. Similarly, a large $\Delta m/m$ reduces the initial heavy fraction in thermal equilibrium. Varying m_l shifts both the onset redshift and the duration of rapid abundance evolution. In all cases, the heavy component is suppressed along with the light component, confirming that gravitational coupling efficiently transfers acoustic suppression from the light sector to the pressureless heavy sector.

5 Constraints

In this section we derive constraints on the parameter space using small-scale structure probes. The Lyman- α forest and high-redshift UV luminosity function constraints are taken from existing works [80, 81] that calibrated their limits against nonlinear simulations but projected them onto the linear matter power spectrum. We apply these recast constraints directly to our linear power spectra. Sec. 5.1 describes the Lyman- α recast, Sec. 5.2 presents the UV luminosity function recast, and Sec. 5.3 combines the exclusions to identify the allowed parameter space.

5.1 Lyman- α forest

The Lyman- α forest consists of neutral-hydrogen absorption lines in quasar spectra at $z \simeq 2$ –5 and is one of the most stringent probes of small-scale matter clustering. State-of-the-art analyses of high-resolution data from XQ-100 [82] and HIRES/MIKE [83] have placed strong lower bounds on the thermal WDM mass [84]: $m_{\text{WDM}} > 5.3 \text{ keV}$ at 95% C.L. from a full MCMC analysis comparing hydrodynamical simulations with observational data.

In this work, we cannot repeat such computationally expensive hydrodynamical simulations for every point in our parameter space, thus we adopt the recast approach validated by Ref. [80]. The central premise is that if a model beyond ΛCDM produces a linear matter

power spectrum with cumulative suppression comparable to that of a 5.3 keV thermal WDM, it will yield statistically indistinguishable Lyman- α fluxes. This approach is particularly well suited to our cases, whose transfer function shape only differs from that of WDM due to the oscillatory features and shallower asymptotic slope discussed in the right panel of Fig. 5.

Following Ref. [80], we first compute the one-dimensional matter power spectrum,

$$P_{1D}(k) = \frac{1}{2\pi} \int_k^\infty dk' k' P(k'), \quad (5.1)$$

and define the suppression estimator

$$A \equiv \int_{k_{\min}}^{k_{\max}} dk \frac{P_{1D}^{\text{model}}(k)}{P_{1D}^{\Lambda\text{CDM}}(k)}, \quad (5.2)$$

with the fractional deficit

$$\delta A \equiv \frac{A_{\Lambda\text{CDM}} - A}{A_{\Lambda\text{CDM}}}. \quad (5.3)$$

We adopt $k_{\min} = 0.5 \text{ h Mpc}^{-1}$ and $k_{\max} = 20 \text{ h Mpc}^{-1}$ to cover the wavenumber range probed by the XQ-100 and HIRES/MIKE data [80, 84]. The exclusion threshold is calibrated by evaluating δA for a thermal relic with $m_{\text{WDM}}^{\text{ref}} = 5.3 \text{ keV}$, yielding

$$\delta A_{\text{crit}} \equiv \delta A(m_{\text{WDM}}^{\text{ref}}) \simeq 0.31. \quad (5.4)$$

The exclusion condition is as follows: any parameter point with $\delta A > \delta A_{\text{crit}}$ is excluded at the 2σ level. We verify that the exclusion region obtained from matching the half-mode scale $k_{1/2}$ (where $\mathcal{T}^2 = 0.5$) is almost identical to this condition for all cross-sections. Therefore, we present only the exclusion derived from this condition.

5.2 High- z UV luminosity functions

High-redshift UV galaxy luminosity functions (UVLFs) offer an independent probe of small-scale matter clustering during cosmic dawn and reionization. UV-selected galaxies at $z \sim 4\text{--}10$ reside in low-mass halos. Their abundance as a function of UV magnitude encodes the halo mass function and indirectly the linear matter power spectrum on comoving scales that are otherwise difficult to access.

We adopt the approach of Ref. [81], which uses current HST UVLF measurements to infer the small-scale matter clustering amplitude after marginalising over astrophysical parameters. Rather than performing a full UVLF likelihood analysis, we recast the model-independent power-spectrum measurements reported therein as constraints on the transfer function $\mathcal{T}^2(k)$. Following Ref. [81], we divide the transfer function into two k bins. The measured amplitudes $a_{s,i}$ relative to ΛCDM are: $a_{s,2} = 0.93_{-0.25}^{+0.34}$ for $0.5 \text{ Mpc}^{-1} \leq k < 2.25 \text{ Mpc}^{-1}$ and $a_{s,3} = 0.66_{-0.17}^{+0.43}$ for $2.25 \text{ Mpc}^{-1} \leq k < 10 \text{ Mpc}^{-1}$, both at 68% CL after marginalisation over all cosmological and astrophysical parameters.

To project our theoretical models onto these constraints, we compute the bin-averaged transfer function to estimate the effective amplitude for each point in our parameter space:

$$\overline{\mathcal{T}_i^2} \equiv \frac{1}{k_{\max,i} - k_{\min,i}} \int_{k_{\min,i}}^{k_{\max,i}} dk \mathcal{T}^2(k). \quad (5.5)$$

We then evaluate this theoretical expectation against the measured posteriors of $a_{s,i}$ in Ref. [81]. Adopting a conservative recasting approach, we exclude any parameter where

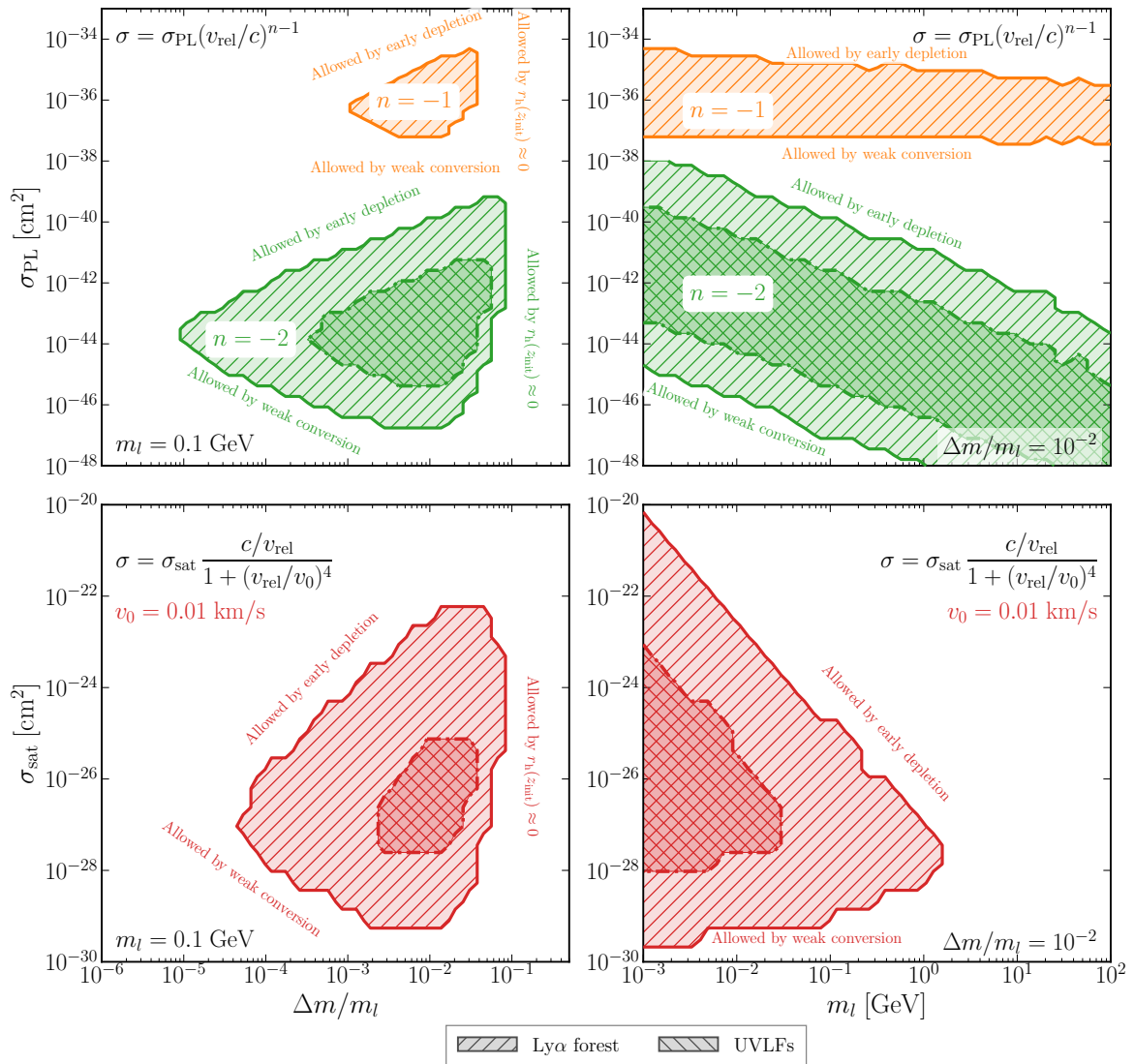


Figure 7. Excluded regions in the $(\Delta m/m_l, \sigma_{\text{PL}}$ and σ_{sat}) plane (left column, $m_l = 0.1$ GeV) and the $(m_l, \sigma_{\text{PL}}$ and σ_{sat}) plane (right column, $\Delta m/m_l = 10^{-2}$) from the Ly- α forest area criterion (/hatched) and high-redshift UVLFs (\-hatched). *Top row:* power-law cross section with $n = -2$ (green) and $n = -1$ (orange). *Bottom row:* Low-velocity saturation cross section with $v_0 = 0.01$ km s $^{-1}$ (red).

the predicted $\overline{\mathcal{T}_i^2}$ falls below the 2σ lower bound of the measured amplitude in either bin (i.e., $\overline{\mathcal{T}_i^2} < a_{s,i} - 2|\sigma_{-,i}|$, where $\sigma_{-,i}$ is the lower uncertainty for $a_{s,i}$).

We would like to emphasise that this UVLF procedure is a recast-level constraint rather than a full UVLF likelihood analysis, which would require an explicit halo model, a galaxy-halo connection, and a consistent marginalisation over astrophysical parameters. Our goal here is to simply examine a given parameter point producing small-scale suppression generically incompatible with current UVLF-inferred clustering. A dedicated likelihood analysis is left to future work.

5.3 Allowed parameter space

Fig. 7 presents the exclusion regions from the Lyman- α (outer contour) and high-redshift UVLFs (inner contour). The top row shows the power-law scenarios ($n = -1$ and $n = -2$), and the bottom row shows the Low-velocity saturation scenarios. In the left panels ($\Delta m/m_l$ vs. σ_{PL} and σ_{sat}), m_l is fixed to 0.1 GeV. In the right panels (m_l vs. σ_{PL} and σ_{sat}), we adopt $\Delta m/m_l = 10^{-2}$.

As discussed in Sec. 4.2, the excluded regions form closed contours, occurring within an intermediate range of cross-section normalization. Below this range, exothermic conversion is too weak to impact perturbations, while above it, the heavy DM species depletes so rapidly that heating ceases. Within certain cross-section, exothermic conversion generates significant pressure support on scales probed by the Lyman- α forest and UVLFs. A similar non-monotonic behavior appears along the $\Delta m/m_l$ axis: at large splittings, exclusion is limited by the exponential suppression of the initial heavy fraction, whereas at small splittings, it is constrained by insufficient energy release per scattering. Clearly, constraints from UVLFs are weaker than those from Lyman- α because they probe larger scales. For the power-law scenario (two upper panels of Fig. 7), the excluded region spans $\sigma_{\text{PL}} \sim 10^{-48}$ to 10^{-40} cm² in the $n = -2$ scenario and $\sigma_{\text{PL}} \sim 10^{-37}$ to 10^{-35} cm² in the $n = -1$ scenario. The $n = -2$ scenario excludes a wider interval of cross sections, owing to its stronger low-velocity enhancement that sustains the conversion process to later times. In contrast, the Low-velocity saturation scenario (two lower panels of Fig. 7) shifts the excluded region to larger cross-section, roughly $\sigma_{\text{sat}} \sim 10^{-30}$ to 10^{-22} cm², because efficient energy conversion is confined to a specific velocity window, requiring a larger cross-section to achieve sufficient total energy injection.

Fig. 8 shows the Lyman- α exclusion in the $(m_l, \Delta m/m_l)$ plane for representative cross sections, namely σ_{PL} (upper panels) and σ_{sat} (lower panels). Larger cross sections shift the excluded region toward smaller $\Delta m/m_l$ and larger m_l , as a higher conversion rate compensates for a smaller energy release or a heavier m_l . However, once the cross-section becomes too large as seen in Fig. 7, the constraining power disappears. The upper boundary of all velocity-dependent cross-sections is determined by the $r_h(z_{\text{init}}) \approx 0$ condition, due to the Boltzmann suppression of the initial heavy fraction. For cross sections with steep velocity dependence ($n = -2$ and the Low-velocity saturation case), low-velocity enhancements amplify the exothermic conversion, leading to nearly identical bounds. In the saturated parametrization, the interaction rate scales as $(v_0/v_{\text{rel}})^4$ when $v_0 \ll v_{\text{rel}}$. Among the three choices of v_0 , the case $v_0 = 0.01$ km s⁻¹ (red solid line) with $\sigma_{\text{sat}} = 10^{-27}$ cm² yields the widest redshift window for efficient conversion, whereas the exclusion regions shrink for $v_0 = 0.001$ km s⁻¹ (blue dashed line) and $v_0 = 0.1$ km s⁻¹ (purple dotted line) due to suppression from the v_0^4 factor and the condition $v_0 \approx v_{\text{rel}}$, respectively. Unlike these two scenarios, the weaker velocity dependence of the $n = -1$ case causes an earlier drop in exothermic conversion, making its exclusions change with respect to σ_{PL} .

In summary, cosmological probes like Lyman- α can constrain certain mass splittings independently of other DM detection methods that rely on interactions with visible particles or dark radiation. In our default setup (inelastic SIDM with thermal initial conditions) and for the most optimistic cases (solid lines) at $m_l \approx 100$ MeV, current Lyman- α data can limit $\Delta m/m_l$ to $\mathcal{O}(10^{-5})$ and $\mathcal{O}(10^{-3})$ for $n = -2$ and $n = -1$, respectively. For the Low-velocity saturation scenarios, the exclusion depends strongly on m_l and v_0 . With the optimistic parameters $\sigma_{\text{sat}} = 10^{-27}$ cm² and $v_0 = 0.01$ km s⁻¹, the largest allowed $\Delta m/m_l$ is $\mathcal{O}(10^{-5})$ for $m_l = 1$ MeV and $\mathcal{O}(10^{-4})$ for $m_l = 10$ MeV.

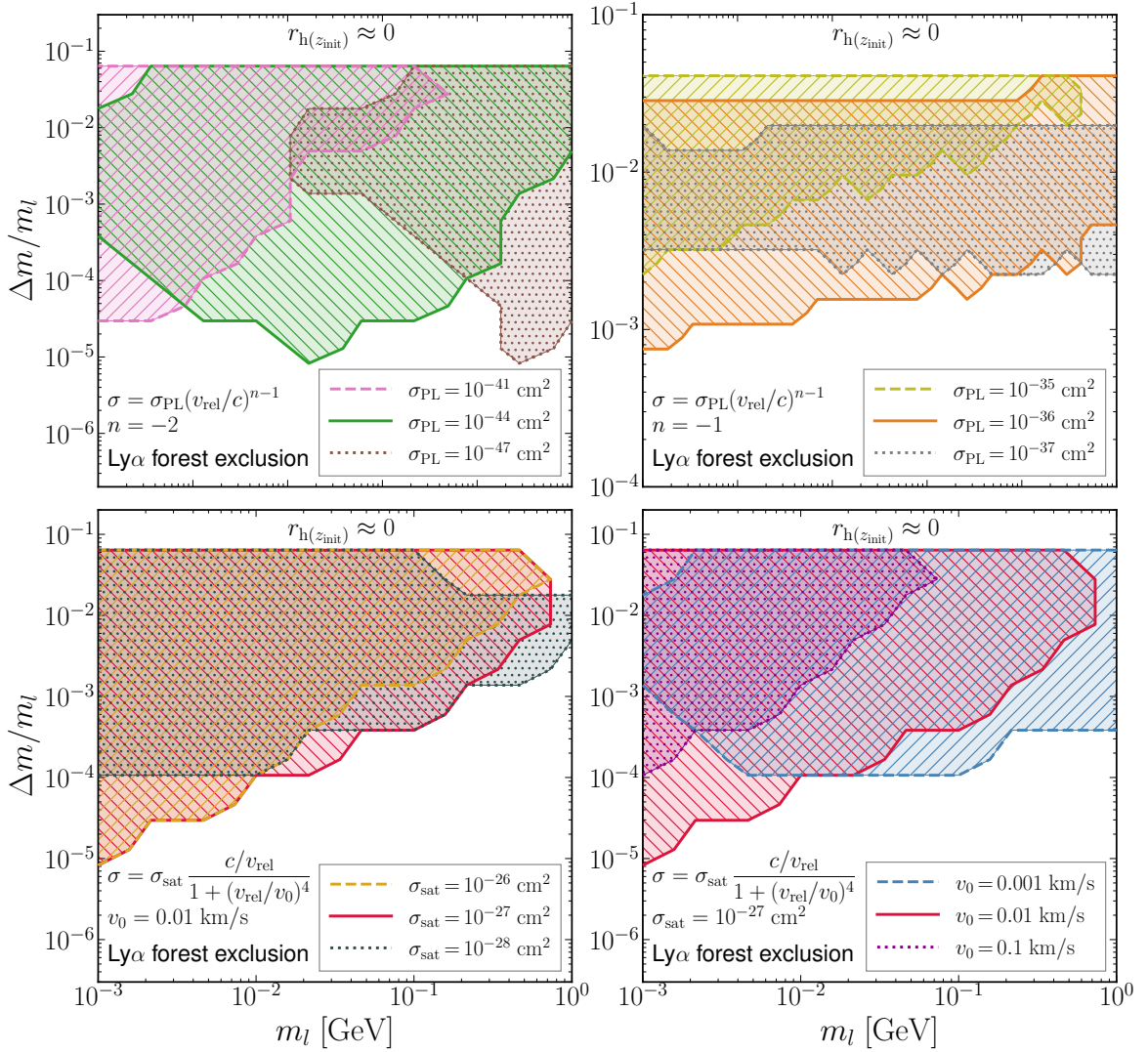


Figure 8. Ly- α forest exclusion in the $(m_l, \Delta m/m_l)$ plane. *Top Left:* Power-law cross section with $n = -2$ ($\sigma_{\text{PL}} = 10^{-41}, 10^{-44}, 10^{-47} \text{ cm}^2$). *Top Right:* Power-law cross section with $n = -1$ ($\sigma_{\text{PL}} = 10^{-35}, 10^{-36}, 10^{-37} \text{ cm}^2$). *Bottom Left:* Low-velocity saturation cross section with fixed $v_0 = 0.01 \text{ km s}^{-1}$ ($\sigma_{\text{sat}} = 10^{-26}, 10^{-27}, 10^{-28} \text{ cm}^2$). *Bottom Right:* Low-velocity saturation cross section with fixed $\sigma_{\text{sat}} = 10^{-27} \text{ cm}^2$ for three transition velocity values ($v_0 = 0.001, 0.01, 0.1 \text{ km s}^{-1}$).

6 Summary and Discussion

In this work, we have investigated the linear cosmological evolution of inelastic SIDM in a two-component dark sector with a small mass splitting Δm . We derived the coupled background and linear perturbation equations for the conversion process $\chi_h \chi_h \leftrightarrow \chi_l \chi_l$, considering both power-law and low-velocity saturation cross sections and using a modified Boltzmann solver based on CLASS.

The homogeneous and perturbation evolution are shaped by the interplay of four parameters. The velocity index n (or saturation velocity v_0) controls the epoch and duration of efficient conversion. The mass splitting $\Delta m/m_l$ plays a dual role, setting the energy release

per conversion while simultaneously suppressing the initial heavy fraction via the Boltzmann factor. The DM mass m_l sets z_{init} and T_{init} , and adjusts departure times of the conversion history. The cross-section normalization governs the overall conversion strength, but an excessively large value causes premature depletion of the heavy species. These competing effects produce non-monotonic parameter dependence throughout. At the perturbation level, conversion-induced heating generates pressure support in the light component. This pressure support, together with conversion-induced drag between the two species, drives acoustic oscillations and suppresses small-scale density growth. The heavy component, though pressureless, is suppressed concurrently through additional friction terms and the weakened gravitational potential. The resulting transfer function features a cutoff at $k \gtrsim 1 h \text{Mpc}^{-1}$ accompanied by DAOs. The visibility of DAOs depends on the cross-section type. Low-velocity saturation scenarios, where conversion terminates abruptly, preserve distinct oscillatory features, whereas power-law cross sections with sustained late-time conversion progressively smooth them out. Compared to thermal WDM matched at the same half-mode scale, the inelastic SIDM transfer function exhibits a shallower high- k suppression tail and the presence of DAOs. The shallower tail reflects the fact that the suppression originates from conversion-induced heating rather than collisionless free streaming. These distinct spectral features offer potential model discrimination.

Using recast constraints from Lyman- α forest data and high-redshift UV luminosity functions, we identified closed exclusion regions driven by the non-monotonic parameter dependences. For the power-law parametrization, the excluded range spans $\sigma_{\text{PL}} \sim 10^{-48}$ – 10^{-40} cm^2 for $n = -2$ and $\sim 10^{-37}$ – 10^{-35} cm^2 for $n = -1$, probing mass splittings down to $\mathcal{O}(10^{-5})$ and $\mathcal{O}(10^{-3})$, respectively. The low-velocity saturation scenario shifts the exclusion to $\sigma_{\text{sat}} \sim 10^{-30}$ – 10^{-22} cm^2 . These results demonstrate that the internal thermodynamics of a secluded dark sector can be constrained purely through its gravitational imprint on structure formation, independent of DM–SM couplings.

Future extensions include N -body simulations with inelastic conversion to capture non-linear evolution and halo formation, exploration of non-thermal initial conditions, and comprehensive MCMC analyses to refine the allowed parameter space. Next generation probes such as 21 cm cosmology and CMB spectral distortion measurements will further extend.

Acknowledgments

We would like to thank Yi Wang, Peizhi Du and Yi-Ming Zhong for insightful discussions. This work is supported in part by the National Science Foundation of China (No. 12588101), the National Key Research and Development Program of China (No. 2022YFF0503304), the Project for Young Scientists in Basic Research of the Chinese Academy of Sciences (No. YSBR-092), and the China Manned Space Program (No. CMS-CSST-2025-A03), the Basic and Frontier Research Project of PCL (grant No. 2025QYB012) and the Major Key project of Peng Cheng Laboratory.

A Appendix

A.1 Thermally averaged conversion rates

For a Maxwell–Boltzmann distribution with temperature T , the thermally averaged product $\langle \sigma v_{\text{rel}} \rangle$ is defined as

$$\langle \sigma v_{\text{rel}} \rangle = \frac{1}{2} \left(\frac{m}{4\pi T} \right)^{3/2} \int_{v_{\text{min}}}^{\infty} \sigma v_{\text{rel}} e^{-mv_{\text{rel}}^2/4T} 4\pi v_{\text{rel}}^2 dv_{\text{rel}}, \quad (\text{A.1})$$

where $m/2$ is the reduced mass of identical particles and $v_{\text{min}} = 0$ for the exothermic channel, $v_{\text{min}} = 2\sqrt{2\Delta m/m_l}$ for the endothermic channel. Substituting the cross-section parameterizations of Sec. 2.1, the conversion rates take the following explicit forms.

- **Power-law parameterization.** Inserting $\sigma = \sigma_{\text{PL}} v_{\text{rel}}^{n-1}$ into Eq. (A.1), and using $\mathcal{R} \equiv a \frac{\rho}{m} \langle \sigma v_{\text{rel}} \rangle$, the exothermic and endothermic conversion rates are

$$\mathcal{R}_d^{\text{PL}} = a \frac{\bar{\rho}_h}{m_h} c_n \sigma_{\text{PL}} \left(\frac{T_h}{m_h} \right)^{n/2}, \quad (\text{A.2})$$

$$\mathcal{R}_u^{\text{PL}} = a \frac{\bar{\rho}_l}{m_l} c_n \sigma_{\text{PL}} \left(\frac{T_l}{m_l} \right)^{n/2} Q \left(\frac{3}{2} + \frac{n}{2}, \frac{2\Delta m}{T_l} \right), \quad (\text{A.3})$$

where

$$c_n \equiv \frac{2^n \Gamma(\frac{3}{2} + \frac{n}{2})}{\sqrt{\pi}} \quad (\text{A.4})$$

is a numerical prefactor from the thermal average, and $Q(x, y) \equiv \Gamma(x, y)/\Gamma(x)$ is the regularised upper incomplete gamma function. The factor Q encodes the kinematic threshold for the endothermic process: $Q \rightarrow 1$ when $\Delta m/T_l \rightarrow 0$ (threshold irrelevant) and $Q \rightarrow 0$ when $\Delta m/T_l \gg 1$ (Boltzmann-suppressed). In the latter limit, \mathcal{R}_u reduces to $\mathcal{R}_d e^{-2\Delta m/T_l}$ up to a power-law prefactor.

- **Low-velocity saturation.** Inserting Eq. (2.2) into Eq. (A.1), the exothermic rate is

$$\mathcal{R}_d^{\text{sat}} = a \frac{\bar{\rho}_h}{m_h} \sigma_{\text{sat}} \left[1 + \left(\frac{3\sqrt{\pi}}{16} \right)^{4/3} \left(\frac{4T_h}{m_h v_0^2} \right)^2 \right]^{-3/4}, \quad (\text{A.5})$$

and the endothermic rate is approximated by

$$\mathcal{R}_u^{\text{sat}} \simeq \mathcal{R}_d^{\text{sat}} e^{-2\Delta m/T_l}. \quad (\text{A.6})$$

This approximation is appropriate because the saturation cross-section targets the low-velocity regime where $\Delta m/T_l \gtrsim 1$; the kinematic threshold then lies deep in the Boltzmann tail, and the exponential factor captures the dominant suppression.

A.2 Evolution of Number Density

We consider a dark sector consisting of two non-relativistic species, denoted as χ_l (light) and χ_h (heavy), which interconvert via the inelastic scattering process:

$$\chi_l \chi_l \leftrightarrow \chi_h \chi_h. \quad (\text{A.7})$$

and assume that each species maintains an approximate Maxwell–Boltzmann distribution characterized by its own temperature T_i (allowing for $T_l \neq T_h$). For the collision term, we account for the symmetry factor of 1/2 for identical initial states and the fact that each reaction event changes the particle number by two. These factors cancel out, allowing the net source terms to be written compactly as $\pm \langle \sigma v \rangle n_i^2$.

In an expanding Friedmann–Robertson–Walker (FRW) background, the Boltzmann equations for the number densities are given by:

$$\dot{n}_l + 3Hn_l = -\langle \sigma v \rangle_{l \rightarrow hh}(T_l) n_l^2 + \langle \sigma v \rangle_{hh \rightarrow l}(T_h) n_h^2, \quad (\text{A.8})$$

$$\dot{n}_h + 3Hn_h = -\langle \sigma v \rangle_{hh \rightarrow l}(T_h) n_h^2 + \langle \sigma v \rangle_{l \rightarrow hh}(T_l) n_l^2. \quad (\text{A.9})$$

For convenience, we define the total number density n_{tot} and the heavy-state fraction r_h as:

$$n_{\text{tot}} \equiv n_l + n_h, \quad r_h \equiv \frac{n_h}{n_{\text{tot}}}. \quad (\text{A.10})$$

Since the total number density scales as $n_{\text{tot}} \propto a^{-3}$ (implying $\dot{n}_{\text{tot}} + 3Hn_{\text{tot}} = 0$), the evolution of the heavy fraction is driven solely by the interaction terms. Combining Eqs. (A.8)–(A.10), we obtain:

$$\dot{r}_h = n_l T_l \langle \sigma v \rangle_{l \rightarrow hh} \times (1 - r_h) - n_h T_h \langle \sigma v \rangle_{hh \rightarrow l} \times r_h. \quad (\text{A.11})$$

It is often convenient to rewrite the evolution in terms of redshift z . Using the relation $dt/dz = -[(1+z)H(z)]^{-1}$, Eq. (A.11) becomes:

$$\frac{dr_h}{dz} = \frac{1}{(1+z)H(z)} [n_h \langle \sigma v \rangle_{hh \rightarrow l}(T_h) r_h - n_l \langle \sigma v \rangle_{l \rightarrow hh}(T_l) (1 - r_h)]. \quad (\text{A.12})$$

A.3 Evolution of Temperature

We model each species as a non-relativistic ideal gas with energy density ρ_i and pressure p_i :

$$\rho_i = m_i n_i + \frac{3}{2} n_i T_i, \quad p_i = n_i T_i. \quad (\text{A.13})$$

Let $U_i \equiv \rho_i V$ be the internal energy in a comoving volume V . According to the first law of thermodynamics,

$$dU_i = -p_i dV + dQ_i, \quad (\text{A.14})$$

where dQ_i represents the heat exchange due to the inelastic conversion. Over a time interval dt , the net energy injected into the light species χ_l is:

$$\frac{dQ_l}{dt} = V \left[\langle \sigma v \rangle_{hh \rightarrow l}(T_h) n_h^2 \left(m_h + \frac{3}{2} T_h \right) - \langle \sigma v \rangle_{l \rightarrow hh}(T_l) n_l^2 \left(m_l + \frac{3}{2} T_l \right) \right]. \quad (\text{A.15})$$

Assuming the dark sector is closed (i.e., no energy loss to other sectors), energy conservation implies $dQ_h/dt = -dQ_l/dt$.

Using an independent internal energy of each species $dU_l = d[n_l V (m_l + 3T_l/2)]$, we obtain

$$\frac{dU_l}{dt} = V \left(m_l + \frac{3}{2} T_l \right) \dot{n}_l + \frac{3}{2} V n_l \dot{T}_l + \left(m_l n_l + \frac{3}{2} n_l T_l \right) \frac{\dot{V}}{V} V. \quad (\text{A.16})$$

Using $\dot{V}/V = 3H$, substituting Eqs. (A.14), (A.15), and (A.16), and utilizing the number density Eq. (A.8), we arrive at the temperature evolution equation for χ_l ,

$$\dot{T}_l = -2HT_l + \frac{2}{3} \langle \sigma v \rangle_{hh \rightarrow l}(T_h) \frac{n_h^2}{n_l} \left[\Delta m + \frac{3}{2} (T_h - T_l) \right]. \quad (\text{A.17})$$

Similarly, for the heavy component χ_h ,

$$\dot{T}_h = -2HT_h - \frac{2}{3}\langle\sigma v\rangle_{ll\rightarrow hh}(T_l)\frac{n_l^2}{n_h}\left[\Delta m + \frac{3}{2}(T_h - T_l)\right]. \quad (\text{A.18})$$

Expressing these in terms of redshift z :

$$\frac{dT_l}{dz} = \frac{2T_l}{1+z} - \frac{2}{3(1+z)H(z)}\frac{n_h^2}{n_l}\langle\sigma v\rangle_{hh\rightarrow ll}(T_h)\left[\Delta m + \frac{3}{2}(T_h - T_l)\right], \quad (\text{A.19})$$

$$\frac{dT_h}{dz} = \frac{2T_h}{1+z} + \frac{2}{3(1+z)H(z)}\frac{n_l^2}{n_h}\langle\sigma v\rangle_{ll\rightarrow hh}(T_l)\left[\Delta m + \frac{3}{2}(T_h - T_l)\right]. \quad (\text{A.20})$$

These equations rely on the assumption of rapid self-thermalization, ensuring each species is described by a single temperature. The term proportional to Δm in Eq. (A.17) represents *chemical heating*: the exothermic de-excitation $hh \rightarrow ll$ converts the mass splitting energy into kinetic energy of the light species. Conversely, the endothermic excitation $ll \rightarrow hh$ acts as a cooling term for the heavy component distribution.

A.4 Derivation of the Linear Perturbation Equations

The derivation is based on the energy–momentum transfer formalism, in which each species satisfies

$$\nabla_\mu {}^{(i)}T^\mu{}_\nu = Q_\nu^{(i)}, \quad i \in \{l, h\}, \quad (\text{A.21})$$

with $\sum_i Q_\nu^{(i)} = 0$ ensuring total energy–momentum conservation.

We work in Newtonian gauge,

$$ds^2 = a^2(\tau) \left[-(1 + 2\Psi)d\tau^2 + (1 - 2\Phi) d\mathbf{x}^2 \right], \quad (\text{A.22})$$

where Ψ and Φ are the metric potentials, τ is conformal time, and $\mathcal{H} \equiv a'/a$ with prime denoting $d/d\tau$. For each species, perturbations are defined by

$$\rho_i(\tau, \mathbf{x}) = \bar{\rho}_i(\tau) [1 + \delta_i(\tau, \mathbf{x})], \quad \theta_i \equiv \partial_j v_i^j, \quad (\text{A.23})$$

where v_i^j is the peculiar velocity. To first order,

$$u_i^0 = \frac{1}{a}(1 - \Psi), \quad u_i^j = \frac{1}{a}v_i^j, \quad u_{i0} = -a(1 + \Psi), \quad u_{ij} \simeq a v_{ij}, \quad (\text{A.24})$$

and the energy–momentum tensor is approximated as an ideal fluid,

$${}^{(i)}T^{\mu\nu} = (\rho_i + p_i)u_i^\mu u_i^\nu + p_i g^{\mu\nu}. \quad (\text{A.25})$$

The collision term in the Boltzmann equation defines the energy–momentum transfer four-vector as the first momentum moment,

$$Q_\nu^{(i)} \equiv \int d\Pi p_\nu C_i[f], \quad (\text{A.26})$$

such that Eq. (A.21) holds. For the inelastic conversion $\chi_h\chi_h \leftrightarrow \chi_l\chi_l$, a minimal covariant form consistent with $\sum_i Q_\nu^{(i)} = 0$ is

$$Q_\nu^{(l)} = +\langle\sigma v\rangle_{hh\rightarrow ll}\frac{\rho_h^2}{m_h}u_\nu^{(h)} - \langle\sigma v\rangle_{ll\rightarrow hh}\frac{\rho_l^2}{m_l}u_\nu^{(l)}, \quad (\text{A.27})$$

$$Q_\nu^{(h)} = -Q_\nu^{(l)}. \quad (\text{A.28})$$

Following Refs. [85, 86], the perturbed conservation equations (A.21) for non-relativistic species ($w_i = 0$) yield the continuity and Euler equations

$$\frac{d\delta_i}{dt} + \frac{\theta_i}{a} + 3\frac{d\Phi}{dt} = \frac{1}{\bar{\rho}_i} \left(\bar{Q}_0^{(i)}|_t \delta_i - Q_0^{(i,1)}|_t \right), \quad (\text{A.29})$$

$$\frac{d\theta_i}{dt} + H\theta_i + \frac{k^2\Psi}{a} + \frac{\delta P_i}{\delta\rho_i} \frac{k^2\delta_i}{a} = \frac{1}{\bar{\rho}_i} \left(\frac{\partial_j Q_j^{(i,1)}|_t}{a} + \bar{Q}_0^{(i)}|_t \theta_i \right), \quad (\text{A.30})$$

where $|_t$ indicates that the transfer components are evaluated with $u_0^{(0)} = -1$.

Expanding Eq. (A.27) to first order using $\rho_i = \bar{\rho}_i(1 + \delta_i)$, the relevant components are

$$\bar{Q}_0^{(l)}|_t = -\langle\sigma v\rangle_{hh\rightarrow ll} \frac{\bar{\rho}_h^2}{m_h} + \langle\sigma v\rangle_{ll\rightarrow hh} \frac{\bar{\rho}_l^2}{m_l}, \quad (\text{A.31})$$

$$Q_0^{(l,1)}|_t = -\langle\sigma v\rangle_{hh\rightarrow ll} \frac{\bar{\rho}_h^2}{m_h} (2\delta_h + \Psi) + \langle\sigma v\rangle_{ll\rightarrow hh} \frac{\bar{\rho}_l^2}{m_l} (2\delta_l + \Psi), \quad (\text{A.32})$$

$$\frac{\partial_j Q_j^{(l,1)}|_t}{a} = \langle\sigma v\rangle_{hh\rightarrow ll} \frac{\bar{\rho}_h^2}{m_h} \theta_h - \langle\sigma v\rangle_{ll\rightarrow hh} \frac{\bar{\rho}_l^2}{m_l} \theta_l. \quad (\text{A.33})$$

Substituting Eqs. (A.31)–(A.33) into Eqs. (A.29)–(A.30) and converting to conformal time via $d/dt = (1/a)d/d\tau$, $H = \mathcal{H}/a$, and the energy density ratio $\xi \equiv \bar{\rho}_h/\bar{\rho}_l$, which is related to the number fraction $r_h \equiv n_h/(n_l + n_h)$ by $\xi = (m_h/m_l)r_h/(1 - r_h)$. The resulting conformal-time perturbation equations are

$$\delta'_l = -\theta_l + 3\Phi' + \xi\mathcal{R}_d(2\delta_h - \delta_l + \Psi) - \mathcal{R}_u(\delta_l + \Psi), \quad (\text{A.34})$$

$$\delta'_h = -\theta_h + 3\Phi' + \frac{1}{\xi}\mathcal{R}_u(2\delta_l - \delta_h + \Psi) - \mathcal{R}_d(\delta_h + \Psi), \quad (\text{A.35})$$

and

$$\theta'_l = -\mathcal{H}\theta_l + k^2\Psi + k^2c_{s,l}^2\delta_l + \xi\mathcal{R}_d(\theta_h - \theta_l), \quad (\text{A.36})$$

$$\theta'_h = -\mathcal{H}\theta_h + k^2\Psi + \frac{1}{\xi}\mathcal{R}_u(\theta_l - \theta_h). \quad (\text{A.37})$$

Equations (A.34)–(A.37) reduce to the standard CDM limit when $\mathcal{R}_d = \mathcal{R}_u = 0$.

A.5 Second-Order Density Perturbation Equations

To analyse the physical regimes discussed in the main text it is useful to have closed second-order equations for δ_l and δ_h in which the velocity divergences have been eliminated. We set $\mathcal{R}_u = 0$ throughout.

- **Heavy component**

From Eq. (A.35) we extract

$$\theta_h = -\delta'_h + 3\Phi' - \mathcal{R}_d(\delta_h + \Psi). \quad (\text{A.38})$$

Differentiating Eq. (A.35) and substituting Eq. (A.37) for θ'_h , then using Eq. (A.38) to eliminate θ_h , we obtain

$$\delta''_h + (\mathcal{H} + \mathcal{R}_d)\delta'_h + (\mathcal{R}_d\mathcal{H} + \mathcal{R}'_d)\delta_h = -k^2\Psi + S_h, \quad (\text{A.39})$$

where the source term depending only on the metric potentials is

$$S_h = -(\mathcal{R}_d \mathcal{H} + \mathcal{R}'_d) \Psi - \mathcal{R}_d \Psi' + 3\Phi'' + 3\mathcal{H}\Phi'. \quad (\text{A.40})$$

The friction coefficient $\mathcal{H} + \mathcal{R}_d$ exceeds the standard Hubble drag by the conversion rate, and the term $(\mathcal{R}_d \mathcal{H} + \mathcal{R}'_d) \delta_h$ acts as an effective dissipation of the heavy-component overdensity.

- **Light component**

From Eq. (A.34) we extract

$$\theta_l = -\delta'_l + 3\Phi' + \xi \mathcal{R}_d (2\delta_h - \delta_l + \Psi). \quad (\text{A.41})$$

The velocity difference follows from Eqs. (A.38) and (A.41),

$$\theta_h - \theta_l = \delta'_l - \delta'_h - \mathcal{R}_d (\delta_h + \Psi) - \xi \mathcal{R}_d (2\delta_h - \delta_l + \Psi). \quad (\text{A.42})$$

Differentiating Eq. (A.34) and substituting Eq. (A.36) for θ'_l , then using Eqs. (A.41) and (A.42) to eliminate θ_l and $\theta_h - \theta_l$, we obtain after collecting terms

$$\delta''_l + (\mathcal{H} + 2\xi \mathcal{R}_d) \delta'_l + \left[\xi \mathcal{R}_d \mathcal{H} + (\xi \mathcal{R}_d)^2 + (\xi \mathcal{R}_d)' + k^2 c_s^2 \right] \delta_l = -k^2 \Psi + S_l, \quad (\text{A.43})$$

where

$$S_l = (\xi \mathcal{R}_d \mathcal{H} + \xi \mathcal{R}_d^2 + (\xi \mathcal{R}_d)^2 + (\xi \mathcal{R}_d)') \Psi + \xi \mathcal{R}_d \Psi' + 3\mathcal{H}\Phi' + 3\Phi'' + 3\xi \mathcal{R}_d \delta'_h + (\xi \mathcal{R}_d^2 + 2(\xi \mathcal{R}_d)' + 2(\xi \mathcal{R}_d) \mathcal{H}) \delta_h. \quad (\text{A.44})$$

Several features of Eq. (A.43) are worth noting. The friction coefficient $\mathcal{H} + 2\xi \mathcal{R}_d$ contains a conversion contribution $2\xi \mathcal{R}_d$ that is twice that appearing in the heavy equation. The additional factor arises from eliminating the velocity difference $\theta_h - \theta_l$. The effective frequency squared of the δ_l mode receives contributions from both the sound speed ($k^2 c_s^2$) and the conversion process ($\xi \mathcal{R}_d \mathcal{H} + (\xi \mathcal{R}_d)^2 + (\xi \mathcal{R}_d)'$). The latter are independent of k and arise purely from the inelastic scattering. The source S_l couples δ_l to δ_h and δ'_h , representing the injection of converted particles from the heavy into the light component.

A.6 Sound Speed and Pressure Perturbations in the Light Sector

In the derivation of the momentum conservation equation for the light DM state χ_l , we introduced a pressure gradient term proportional to an effective sound speed squared, $c_{s,l}^2$. Given that the exothermic conversion $hh \rightarrow ll$ significantly alters the thermal history of the light sector, causing it to deviate from standard adiabatic cooling, care must be taken in defining the sound speed. The adiabatic sound speed, $c_{a,l}^2$, is strictly defined by the evolution of the background pressure \bar{P}_l and density $\bar{\rho}_l$ as $c_{a,l}^2 \equiv \dot{\bar{P}}_l / \dot{\bar{\rho}}_l$. Assuming the light component maintains local thermal equilibrium and behaves as a non-relativistic ideal gas, this definition yields

$$c_{a,l}^2(\tau) = \frac{T_l}{m_l} \left(1 - \frac{1}{3} \frac{d \ln T_l}{d \ln a} \right). \quad (\text{A.45})$$

This expression governs the evolution of the fluid stiffness, incorporating chemical heating effects through the modified temperature slope $d \ln T_l / d \ln a$.

The sound speed appearing in the perturbation equations, often called as the effective sound speed $c_{\text{eff}}^2 \equiv \delta P_l / \delta \rho_l$, is generally frame-dependent. It is physically useful to relate c_{eff}^2 to the rest-frame sound speed $\hat{c}_{s,l}^2$, which describes the intrinsic pressure response to density fluctuations. In the Newtonian gauge, this relation is given by a gauge transformation of the pressure perturbation δP_l ,

$$\delta P = c_a^2 \delta \rho + (\hat{c}_s^2 - c_a^2) (\delta \rho - \dot{\rho} \frac{\theta}{k^2}). \quad (\text{A.46})$$

This implies that the effective sound speed in the calculation frame differs from the rest-frame value by a term proportional to $(\hat{c}_{s,l}^2 - c_{a,l}^2)$ and the velocity divergence.

In our analysis, we adopt the standard fluid approximation by identifying the effective sound speed with the adiabatic sound speed, $c_{s,l}^2 \approx \hat{c}_{s,l}^2 \approx c_{a,l}^2$. This approximation assumes local thermal equilibrium: despite vigorous energy injection from the heavy sector, the light DM particles maintain (or rapidly relax to) a local Maxwell-Boltzmann distribution with temperature $T(\mathbf{x}) = \bar{T} + \delta T$. Under this condition, the rest-frame pressure perturbation follows the background instantaneous adiabatic relation.

Any deviations from this adiabatic response (i.e., intrinsic entropy perturbations) are treated as sub-dominant in the fluid limit. Furthermore, distinct from the intrinsic sound speed of the light component, the *relative entropy perturbations* between the heavy and light sectors (arising from their distinct evolution) are explicitly governed by the interaction terms in the coupled Boltzmann equations (Eqs. (2.8)–(2.10)). Consequently, the pressure gradient term in Eq. (2.10) describes the internal hydrodynamical dynamics of the light fluid, consistently measured by the adiabatic sound speed in Eq. (A.45).

References

- [1] S.D.M. White and M.J. Rees, *Core condensation in heavy halos: A Two stage theory for galaxy formation and clusters*, *Mon. Not. Roy. Astron. Soc.* **183** (1978) 341.
- [2] G.R. Blumenthal, S.M. Faber, J.R. Primack and M.J. Rees, *Formation of Galaxies and Large Scale Structure with Cold Dark Matter*, *Nature* **311** (1984) 517.
- [3] J.F. Navarro, C.S. Frenk and S.D.M. White, *The Structure of cold dark matter halos*, *Astrophys. J.* **462** (1996) 563 [[astro-ph/9508025](#)].
- [4] XENON collaboration, *First Dark Matter Search with Nuclear Recoils from the XENONnT Experiment*, *Phys. Rev. Lett.* **131** (2023) 041003 [[2303.14729](#)].
- [5] PANDAX collaboration, *Dark Matter Search Results from 1.54 Tonne-Year Exposure of PandaX-4T*, *Phys. Rev. Lett.* **134** (2025) 011805 [[2408.00664](#)].
- [6] DARKSIDE-50 collaboration, *Search for low-mass dark matter WIMPs with 12 ton-day exposure of DarkSide-50*, *Phys. Rev. D* **107** (2023) 063001 [[2207.11966](#)].
- [7] CDEX collaboration, *Limits on Light Weakly Interacting Massive Particles from the First 102.8 kg × day Data of the CDEX-10 Experiment*, *Phys. Rev. Lett.* **120** (2018) 241301 [[1802.09016](#)].
- [8] A. Boveia and C. Doglioni, *Dark Matter Searches at Colliders*, *Ann. Rev. Nucl. Part. Sci.* **68** (2018) 429 [[1810.12238](#)].
- [9] F. Kahlhoefer, *Review of LHC Dark Matter Searches*, *Int. J. Mod. Phys. A* **32** (2017) 1730006 [[1702.02430](#)].
- [10] O. Buchmueller, C. Doglioni and L.T. Wang, *Search for dark matter at colliders*, *Nature Phys.* **13** (2017) 217 [[1912.12739](#)].

- [11] M. Pospelov, A. Ritz and M.B. Voloshin, *Secluded WIMP Dark Matter*, *Phys. Lett. B* **662** (2008) 53 [0711.4866].
- [12] N. Arkani-Hamed, D.P. Finkbeiner, T.R. Slatyer and N. Weiner, *A Theory of Dark Matter*, *Phys. Rev. D* **79** (2009) 015014 [0810.0713].
- [13] Y. Hochberg, E. Kuflik, T. Volansky and J.G. Wacker, *Mechanism for Thermal Relic Dark Matter of Strongly Interacting Massive Particles*, *Phys. Rev. Lett.* **113** (2014) 171301 [1402.5143].
- [14] F.-Y. Cyr-Racine, K. Sigurdson, J. Zavala, T. Bringmann, M. Vogelsberger and C. Pfrommer, *ETHOS—an effective theory of structure formation: From dark particle physics to the matter distribution of the Universe*, *Phys. Rev. D* **93** (2016) 123527 [1512.05344].
- [15] V. Poulin, P.D. Serpico and J. Lesgourgues, *A fresh look at linear cosmological constraints on a decaying dark matter component*, *JCAP* **08** (2016) 036 [1606.02073].
- [16] C. Boehm, M.J. Dolan and C. McCabe, *A Lower Bound on the Mass of Cold Thermal Dark Matter from Planck*, *JCAP* **08** (2013) 041 [1303.6270].
- [17] N. Sabti, J. Alvey, M. Escudero, M. Fairbairn and D. Blas, *Refined Bounds on MeV-scale Thermal Dark Sectors from BBN and the CMB*, *JCAP* **01** (2020) 004 [1910.01649].
- [18] R.A. Flores and J.R. Primack, *Observational and theoretical constraints on singular dark matter halos*, *Astrophys. J. Lett.* **427** (1994) L1 [astro-ph/9402004].
- [19] B. Moore, *Evidence against dissipationless dark matter from observations of galaxy haloes*, *Nature* **370** (1994) 629.
- [20] M. Boylan-Kolchin, J.S. Bullock and M. Kaplinghat, *Too big to fail? The puzzling darkness of massive Milky Way subhaloes*, *Mon. Not. Roy. Astron. Soc.* **415** (2011) L40 [1103.0007].
- [21] J.S. Bullock and M. Boylan-Kolchin, *Small-Scale Challenges to the Λ CDM Paradigm*, *Ann. Rev. Astron. Astrophys.* **55** (2017) 343 [1707.04256].
- [22] K.A. Oman et al., *The unexpected diversity of dwarf galaxy rotation curves*, *Mon. Not. Roy. Astron. Soc.* **452** (2015) 3650 [1504.01437].
- [23] D. Yang and H.-B. Yu, *Self-interacting dark matter and rotation curves of low-mass spirals*, *2306.01830*.
- [24] D. Yang and H.-B. Yu, *Self-interacting dark matter and the origin of rotation curves in low-mass spirals*, *JCAP* **2009** (2020) 077 [2002.02102].
- [25] D.N. Spergel and P.J. Steinhardt, *Observational evidence for selfinteracting cold dark matter*, *Phys. Rev. Lett.* **84** (2000) 3760 [astro-ph/9909386].
- [26] M. Kaplinghat, S. Tulin and H.-B. Yu, *Dark Matter Halos as Particle Colliders: Unified Solution to Small-Scale Structure Puzzles from Dwarfs to Clusters*, *Phys. Rev. Lett.* **116** (2016) 041302 [1508.03339].
- [27] S. Tulin and H.-B. Yu, *Dark Matter Self-interactions and Small Scale Structure*, *Phys. Rept.* **730** (2018) 1 [1705.02358].
- [28] J.L. Feng, M. Kaplinghat and H.-B. Yu, *Halo Shape and Relic Density Exclusions of Sommerfeld-Enhanced Dark Matter Explanations of Cosmic Ray Excesses*, *Phys. Rev. Lett.* **104** (2010) 151301 [0911.0422].
- [29] A. Loeb and N. Weiner, *Cores in Dwarf Galaxies from Dark Matter with a Yukawa Potential*, *Phys. Rev. Lett.* **106** (2011) 171302 [1011.6374].
- [30] S. Tulin, H.-B. Yu and K.M. Zurek, *Beyond Collisionless Dark Matter: Particle Physics Dynamics for Dark Matter Halo Structure*, *Phys. Rev. D* **87** (2013) 115007 [1302.3898].

- [31] E. Del Nobile, M. Kaplinghat and H.-B. Yu, *Direct Detection Signatures of Self-Interacting Dark Matter with a Light Mediator*, *JCAP* **10** (2015) 055 [[1507.04007](#)].
- [32] M. Kaplinghat, S. Tulin and H.-B. Yu, *Direct Detection Portals for Self-interacting Dark Matter*, *Phys. Rev. D* **89** (2014) 035009 [[1310.7945](#)].
- [33] D. Tucker-Smith and N. Weiner, *Inelastic dark matter*, *Phys. Rev. D* **64** (2001) 043502 [[hep-ph/0101138](#)].
- [34] D.P. Finkbeiner and N. Weiner, *Exciting Dark Matter and the INTEGRAL/SPI 511 keV signal*, *Phys. Rev. D* **76** (2007) 083519 [[astro-ph/0702587](#)].
- [35] M. Blennow, S. Clementz and J. Herrero-Garcia, *Self-interacting inelastic dark matter: A viable solution to the small scale structure problems*, *JCAP* **03** (2017) 048 [[1612.06681](#)].
- [36] M. Meneghetti et al., *An excess of small-scale gravitational lenses observed in galaxy clusters*, *Science* **369** (2020) 1347 [[2009.04471](#)].
- [37] R. Essig, S.D. McDermott, H.-B. Yu and Y.-M. Zhong, *Constraining Dissipative Dark Matter Self-Interactions*, *Phys. Rev. Lett.* **123** (2019) 121102 [[1809.01144](#)].
- [38] D. Yang and H.-B. Yu, *Self-interacting dark matter and small-scale gravitational lenses in galaxy clusters*, *Phys. Rev. D* **104** (2021) 103031 [[2102.02375](#)].
- [39] S. Banerjee, S. Matsumoto, K. Mukaida and Y.-L.S. Tsai, *WIMP Dark Matter in a Well-Tempered Regime: A case study on Singlet-Doublets Fermionic WIMP*, *JHEP* **11** (2016) 070 [[1603.07387](#)].
- [40] G.H. Duan, K.-I. Hikasa, J. Ren, L. Wu and J.M. Yang, *Probing bino-wino coannihilation dark matter below the neutrino floor at the LHC*, *Phys. Rev. D* **98** (2018) 015010 [[1804.05238](#)].
- [41] Y.-L.S. Tsai, C.-T. Lu and V.Q. Tran, *Confronting dark matter co-annihilation of Inert two Higgs Doublet Model with a compressed mass spectrum*, *JHEP* **06** (2020) 033 [[1912.08875](#)].
- [42] J.-C. Feng, X.-W. Kang, C.-T. Lu, Y.-L.S. Tsai and F.-S. Zhang, *Revising inelastic dark matter direct detection by including the cosmic ray acceleration*, *JHEP* **04** (2022) 080 [[2110.08863](#)].
- [43] Y.-Z. Fan, T.-P. Tang, Y.-L.S. Tsai and L. Wu, *Inert Higgs Dark Matter for CDF II W-Boson Mass and Detection Prospects*, *Phys. Rev. Lett.* **129** (2022) 091802 [[2204.03693](#)].
- [44] B. Fuks, M.D. Goodsell and T. Murphy, *Monojets from compressed weak frustrated dark matter*, *Phys. Rev. D* **111** (2025) 055010 [[2409.03014](#)].
- [45] D. Yang, Y.-Z. Fan, S. Hou and Y.-L.S. Tsai, *Self-interacting dark matter with mass segregation: a unified explanation of dwarf cores and small-scale lenses*, *Sci. Bull.* **71** (2026) 1349 [[2506.14898](#)].
- [46] D. Yang, Y.-L.S. Tsai and Y.-Z. Fan, *Diversifying halo structures in two-component self-interacting dark matter models via mass segregation*, *Phys. Rev. D* **112** (2025) 083011 [[2504.02303](#)].
- [47] R. Huo, H.-B. Yu and Y.-M. Zhong, *The structure of dissipative dark matter halos*, *JCAP* **06** (2020) 051 [[1912.06757](#)].
- [48] X. Shen, P.F. Hopkins, L. Necib, F. Jiang, M. Boylan-Kolchin and A. Wetzel, *Dissipative dark matter on fire: I. structural and kinematic properties of dwarf galaxies*, *Mon. Not. Roy. Astron. Soc.* **506** (2021) 4421 [[2102.09580](#)].
- [49] X. Shen, P.F. Hopkins, L. Necib, F. Jiang, M. Boylan-Kolchin and A. Wetzel, *Dissipative dark matter on fire: II. observational signatures and constraints from local dwarf galaxies*, *Astrophys. J.* **966** (2024) 131 [[2206.05327](#)].
- [50] S. Adhikari, A. Banerjee, B. Jain, T.H. Shin and Y.-M. Zhong, *Constraints on dark matter self-interactions from weak lensing of galaxies from the dark energy survey around clusters from the atacama cosmology telescope survey*, [2401.05788](#).

- [51] M. Vogelsberger, J. Zavala, K. Schutz and T.R. Slatyer, *Evaporating the milky way halo and its satellites with inelastic self-interacting dark matter*, *Mon. Not. Roy. Astron. Soc.* **484** (2019) 5437 [[1805.03203](#)].
- [52] K.T.E. Chua, K. Dibert, M. Vogelsberger and J. Zavala, *The impact of inelastic self-interacting dark matter on the dark matter structure of a milky way halo*, *Mon. Not. Roy. Astron. Soc.* **500** (2021) 1531 [[2010.08562](#)].
- [53] S. O’Neil, M. Vogelsberger, S. Heeba, K. Schutz, J.C. Rose, P. Torrey et al., *Endothermic self-interacting dark matter in milky way-like dark matter haloes*, *Mon. Not. Roy. Astron. Soc.* **524** (2023) 288 [[2210.16328](#)].
- [54] V. Semenov, S. Pilipenko, A. Doroshkevich, V. Lukash and E. Mikheeva, *Dark matter halo formation in the multicomponent dark matter models*, [1306.3210](#).
- [55] K. Todoroki and M.V. Medvedev, *Dark matter haloes in the multicomponent model. i. substructure*, *Mon. Not. Roy. Astron. Soc.* **483** (2019) 3983 [[1711.11078](#)].
- [56] K. Todoroki and M.V. Medvedev, *Dark matter haloes in the multicomponent model. ii. density profiles of galactic haloes*, *Mon. Not. Roy. Astron. Soc.* **483** (2019) 4004 [[1711.11085](#)].
- [57] K. Todoroki and M.V. Medvedev, *Dark matter haloes in the multicomponent model. iii. from dwarfs to galaxy clusters*, *Mon. Not. Roy. Astron. Soc.* **510** (2022) 4249 [[2003.11096](#)].
- [58] F.-Y. Cyr-Racine and K. Sigurdson, *The cosmology of atomic dark matter*, *Phys. Rev. D* **87** (2013) 103515 [[1209.5752](#)].
- [59] S. Roy, X. Shen, M. Lisanti, D. Curtin, N. Murray and P.F. Hopkins, *Simulating atomic dark matter in milky way analogues*, *Astrophys. J. Lett.* **954** (2023) L40 [[2304.09878](#)].
- [60] S. Roy, X. Shen, J. Barron, M. Lisanti, D. Curtin, N. Murray et al., *Aggressively-dissipative dark dwarfs: The effects of atomic dark matter on the inner densities of isolated dwarf galaxies*, *Astrophys. J.* **982** (2025) 175 [[2408.15317](#)].
- [61] C. Gemmell, S. Roy, X. Shen, D. Curtin, M. Lisanti, N. Murray et al., *Dissipative dark substructure: The consequences of atomic dark matter on milky way analog subhalos*, *Astrophys. J.* **967** (2024) 21 [[2311.02148](#)].
- [62] J.H. Kim, K. Kong, S.H. Lim and J.-C. Park, *Astrophysical and cosmological probes of boosted dark matter*, [2410.05382](#).
- [63] D. Tucker-Smith and N. Weiner, *The status of inelastic dark matter*, *Phys. Rev. D* **72** (2005) 063509 [[hep-ph/0402065](#)].
- [64] S. Chang, G.D. Kribs, D. Tucker-Smith and N. Weiner, *Inelastic dark matter in light of dama/libra*, *Phys. Rev. D* **79** (2009) 043513 [[0807.2250](#)].
- [65] A. De Simone, V. Sanz and H.P. Sato, *Pseudo-Dirac Dark Matter Leaves a Trace*, *Phys. Rev. Lett.* **105** (2010) 121802 [[1004.1567](#)].
- [66] P. Konar, A. Mukherjee, A.K. Saha and S. Show, *Linking pseudo-Dirac dark matter to radiative neutrino masses in a singlet-doublet scenario*, *Phys. Rev. D* **102** (2020) 015024 [[2001.11325](#)].
- [67] M. Baumgart, C. Cheung, J.T. Ruderman, L.-T. Wang and I. Yavin, *Non-Abelian Dark Sectors and Their Collider Signatures*, *JHEP* **04** (2009) 014 [[0901.0283](#)].
- [68] A. Katz and R. Sundrum, *Breaking the dark force*, *JHEP* **06** (2009) 003 [[0902.3271](#)].
- [69] F. Chen, V. Takhistov, N. Weiner and I. Yavin, *Probing a dark sector through the higgs portal*, *JHEP* **01** (2010) 057 [[0907.4746](#)].
- [70] H.-B. Zhang et al., *A non-abelian dark matter model for 511 keV gamma rays and direct detection*, *Phys. Lett. B* **684** (2010) 201 [[0910.2831](#)].

- [71] R. Iengo, *Sommerfeld enhancement: general results from field theory diagrams*, *JHEP* **05** (2009) 024 [[0902.0688](#)].
- [72] K. Griest and M. Kamionkowski, *Unitarity limits on the mass and radius of dark-matter particles*, *Phys. Rev. Lett.* **64** (1990) 615.
- [73] S. Cassel, *Sommerfeld factor for arbitrary partial wave processes*, *J. Phys. G* **37** (2010) 105009 [[0903.5307](#)].
- [74] D. Blas, J. Lesgourgues and T. Tram, *The Cosmic Linear Anisotropy Solving System (CLASS). Part II: Approximation schemes*, *JCAP* **07** (2011) 034 [[1104.2933](#)].
- [75] Planck Collaboration, N. Aghanim et al., *Planck 2018 results. VI. Cosmological parameters*, *Astron. Astrophys.* **641** (2020) A6 [[1807.06209](#)].
- [76] T. Bringmann and S. Hofmann, *Thermal relics, observational hints, and the nature of dark matter*, *JCAP* **04** (2007) 016 [[hep-ph/0612169](#)].
- [77] P. Gondolo and G. Gelmini, *Cosmic abundances of stable particles: Improved analysis*, *Nucl. Phys. B* **360** (1991) 145.
- [78] C.-P. Ma and E. Bertschinger, *Cosmological perturbation theory in the synchronous and conformal Newtonian gauges*, *Astrophys. J.* **455** (1995) 7 [[astro-ph/9506072](#)].
- [79] M. Viel, J. Lesgourgues, M.G. Haehnelt, S. Matarrese and A. Riotto, *Constraining warm dark matter candidates including sterile neutrinos and light gravitinos with WMAP and the Lyman- α forest*, *Phys. Rev. D* **71** (2005) 063534 [[astro-ph/0501562](#)].
- [80] R. Murgia, V. Iršič and M. Viel, *Novel constraints on non-cold (non-thermal) Dark Matter from Lyman- α forest data*, *Phys. Rev. D* **98** (2018) 083540 [[1806.08371](#)].
- [81] N. Sabti, J.B. Muñoz and D. Blas, *New Roads to the Small-Scale Universe: Measurements of the Clustering of Matter with the High-Redshift UV Galaxy Luminosity Function*, *Astrophys. J. Lett.* **928** (2022) L20 [[2110.13161](#)].
- [82] S. López et al., *XQ-100: A legacy survey of one hundred $3.5 \lesssim z \lesssim 4.5$ quasars observed with VLT/X-shooter*, *Astron. Astrophys.* **594** (2016) A91 [[1607.08776](#)].
- [83] M. Viel, G.D. Becker, J.S. Bolton and M.G. Haehnelt, *Warm Dark Matter as a solution to the small scale crisis: New constraints from high redshift Lyman- α forest data*, *Phys. Rev. D* **88** (2013) 043502 [[1306.2314](#)].
- [84] V. Iršič et al., *New Constraints on the free-streaming of warm dark matter from intermediate and small scale Lyman- α forest data*, *Phys. Rev. D* **96** (2017) 023522 [[1702.01764](#)].
- [85] K. Redmond, A. Trezza and A.L. Erickcek, *Growth of Dark Matter Perturbations during Kination*, *Phys. Rev. D* **98** (2018) 063504 [[1807.01327](#)].
- [86] A.L. Erickcek, *The Dark Matter Annihilation Boost from Low-Temperature Reheating*, *Phys. Rev. D* **92** (2015) 103505 [[1504.03335](#)].